4-15-2013

The First Second of Volcanic Eruptions from the Erebus Volcano Lava Lake, Antarctica—Energies, Pressures, Seismology, and Infrasound

A. Gerst
University of Hamburg

M. Hort
University of Hamburg

R. C. Aster
New Mexico Institute of Mining and Technology

J. B. Johnson
Boise State University

P. R. Kyle
New Mexico Institute of Mining and Technology

 DOI: 10.1002/jgrb.50234.

The first second of volcanic eruptions from the Erebus volcano lava lake, Antarctica—Energies, pressures, seismology, and infrasound

A. Gerst,[1,2] M. Hort,[1] R. C. Aster,[3,4] J. B. Johnson,[3,5] and P. R. Kyle[3]

Received 27 May 2013; accepted 30 May 2013; published 15 July 2013.

[1] We describe a multiparameter experiment at Erebus volcano, Antarctica, employing Doppler radar, video, acoustic, and seismic observations to estimate the detailed energy budget of large (up to 40 m-diameter) bubble bursts from a persistent phonolite lava lake. These explosions are readily studied from the crater rim at ranges of less than 500 m and present an ideal opportunity to constrain the dynamics and mechanism of magmatic bubble bursts that can drive Strombolian and Hawaiian eruptions. We estimate the energy budget of the first second of a typical Erebus explosion as a function of time and energy type. We constrain gas pressures and forces using an analytic model for the expansion of a gas bubble above a conduit that incorporates conduit geometry and magma and gas parameters. The model, consistent with video and radar observations, invokes a spherical bulging surface with a base diameter equal to that of the lava lake. The model has no ad hoc free parameters, and geometrical calculations predict zenith height, velocity, and acceleration during shell expansion. During explosions, the energy contained in hot overpressured gas bubbles is freed and partitioned into other energy types, where by far the greatest nonthermal energy component is the kinetic and gravitational potential energy of the accelerated magma shell ($> 10^9$ J). Seismic source energy created by explosions is estimated from radar measurements and is consistent with source energy determined from seismic observations. For the generation of the infrasonic signal, a dual mechanism incorporating a terminally disrupted slug is proposed, which clarifies previous models and provides good fits to observed infrasonic pressures. A new and straightforward method is presented for determining gas volumes from slug explosions at volcanoes from remote infrasound recordings.

Citation: Gerst, A., M. Hort, R. C. Aster, J. B. Johnson, and P. R. Kyle (2013), The first second of volcanic eruptions from the Erebus volcano lava lake, Antarctica—Energies, pressures, seismology, and infrasound, *J. Geophys. Res. Solid Earth*, *118*, 3318–3340, doi:10.1002/jgrb.50234.

1. Introduction

[2] Volcanoes display a wide variety of eruption styles, ranging from the relatively simple discrete explosions analyzed here to massive and sustained Plinian events. The bursting of overpressured bubbles of gas within the magma is key to understanding eruptions. At some volcanoes, repeating explosions in low- to moderate-viscosity magma can be clearly observed with an array of multidisciplinary instrumentation. In these systems, large overpressured bubbles of exsolved gas rise buoyantly within the conduit and rapidly expand upon reaching the surface. This final phase of expansion manifests itself as an explosion within a magma conduit or at a lava lake surface (Figure 1). The rapid expansion and bursting of bubbles in lower viscosity magmas is the key process that drives Strombolian and Hawaiian eruptions [*Vergniolle and Mangan*, 2000; *Vergniolle and Brandeis*, 1994; *Vergniolle et al.*, 1996].

[3] Although such eruptions are simple to conceptualize, detailed constraints on gas overpressures and energy budgets in the explosions are difficult to quantify. Because of its fundamental nature [e.g., *McGetchin and Chouet*, 1979], a number of studies have constrained elements of this type of eruption, principally through the interpretation of seismic [*Neuberg et al.*, 1994; *Chouet et al.*, 1997; *Aster et al.*, 2004a, 2008] and/or infrasound observations [*Ripepe et al.*, 1993; *Vergniolle and Brandeis*, 1994; *Hagerty et al.*, 2000; *Johnson and Lees*, 2000; *Rowe et al.*, 2000; *Garcés et al.*, 2003; *Ripepe et al.*, 2004; *Johnson et al.*, 2004; *Harris and*

Additional supporting information may be found in the online version of this article.

[1]Institute of Geophysics, University of Hamburg, Hamburg, Germany.
[2]Now at the European Astronaut Centre, European Space Agency, Cologne, Germany.
[3]Department of Earth and Environmental Science, New Mexico Institute of Mining and Technology, Socorro, New Mexico, USA.
[4]Geosciences Department, Colorado State University, Fort Collins, Colorado, USA.
[5]Now at the Department of Geosciences, Boise State University, Boise, Idaho, USA.

Corresponding author: M. Hort, Institute of Geophysics, University of Hamburg, Bundesstr. 55, D-20146 Hamburg, Germany. (matthias.hort@zmaw.de)

2169-9313/13/10.1002/jgrb.50234

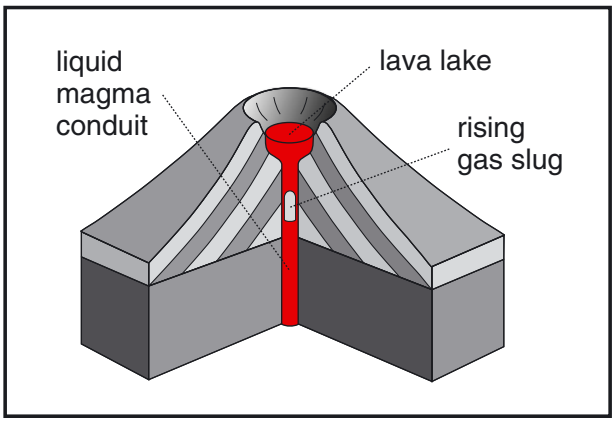

Figure 1. Conceptual illustration of a Strombolian volcano with an open, magma-filled conduit system, in this case with a lava lake at the conduit terminus. Explosions occur when elongated pressurized gas slugs buoyantly rise in the conduit and burst at the top.

Ripepe, 2007; *Johnson and Ripepe*, 2011]. However, such signals only partially characterize the eruption process and associated energies [*Johnson et al.*, 2005; *Vidal et al.*, 2006], and fundamentals such as the mechanism of bubble burst and infrasound generation are still ambiguous [*Vergniolle and Brandeis*, 1994; *Garcés and McNutt*, 1997; *Ripepe and Marchetti*, 2002; *Johnson*, 2003; *Lane and Gilbert*, 2008; *Taddeucci et al.*, 2012; *Del Bello et al.*, 2012]. We report on a multiparameter experiment at Erebus volcano in Antarctica between 15 December 2005 and 2 January 2006 to resolve the phenomenological details and energy balance during the first second of impulsive large magma bubble bursts from an exceptionally well-exposed lava lake.

1.1. Multidisciplinary Observations at Erebus Volcano, Antarctica

[4] While the exact mechanisms and conditions controlling bubble formation and coalescence at depth are still debated [e.g., *Parfitt*, 2004; *Oppenheimer et al.*, 2011] and is not directly relevant for our study, seismic moment tensors at Erebus suggest a formation region for large slugs at a depth of around 400 m below the lava lake [*Aster et al.*, 2008] within a complex underlying magmatic conduit geometry [*Chaput et al.*, 2012; *Zandomeneghi et al.*, 2013]. From the exsolution region that is several kilometers deep [*Oppenheimer et al.*, 2011], the gas rises and ultimately coalesces into large elongated buoyant bubbles (slugs) that fill most of the conduit and rapidly expand upon rising, producing bubble burst explosions at the surface that have been generally characterized as Strombolian eruptions [e.g., *Kyle*, 1994; *Aster et al.*, 2003; *Dibble et al.*, 2008; *Oppenheimer et al.*, 2011; *Molina et al.*, 2012; *Zandomeneghi et al.*, 2013]. This study focuses on the dynamics of the uppermost (< 100 m depth) part of the gas rise in the conduit during this process.

[5] The top of the magma conduit at Erebus volcano forms a long-lived ~1000°C convecting phonolitic lava lake [*Kyle*, 1994; *Oppenheimer and Kyle*, 2008; *Molina et al.*, 2012] with a thin crust that is continually fissuring and remelting. This exposed and self-reconstructing eruptive system can be easily observed from the crater rim at

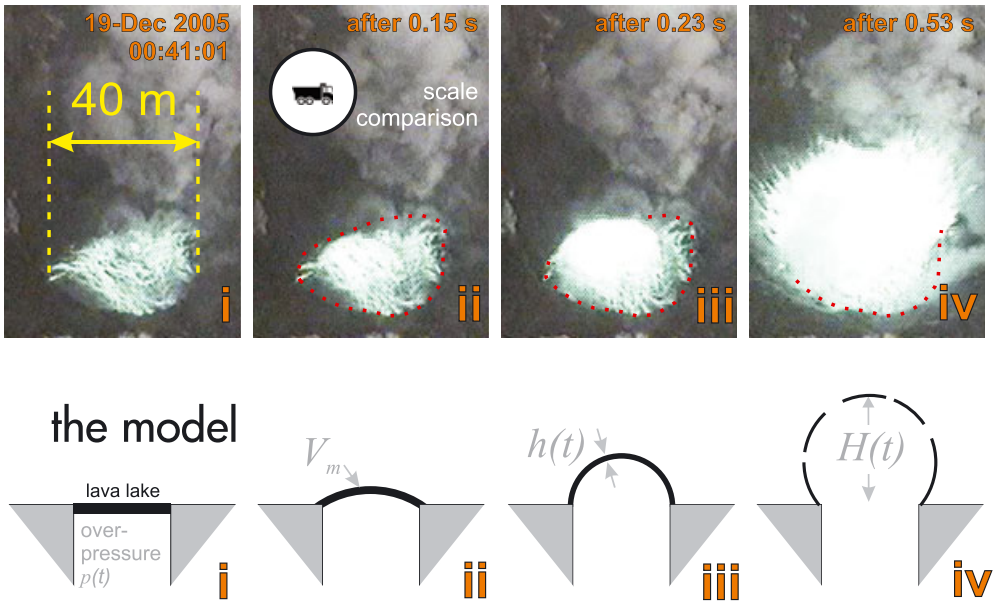

Figure 2. *Bubble model*. (top) Explosion video snapshot sequence, recorded by an infrared-sensitive video camera at Erebus volcano (false color). All four images were recorded within 1 s (times indicated at top), and each represent an evolutionary explosion stage. Note the sketch of a ~10 m mining truck in (ii) for scale comparison. (bottom) Sketch of the eruption model used for the calculation of energies and pressures, which assumes a uniformly expanding magma shell of constant magma volume, driven by underlying pressurized gas. The shell, which is always approximated by a circular section of a sphere (Figure A2), starts out as (episode i) a flat interface evolving into (iii) a hemisphere, before it eventually bursts (between iii and iv, see also Movie S3 in the supporting information).

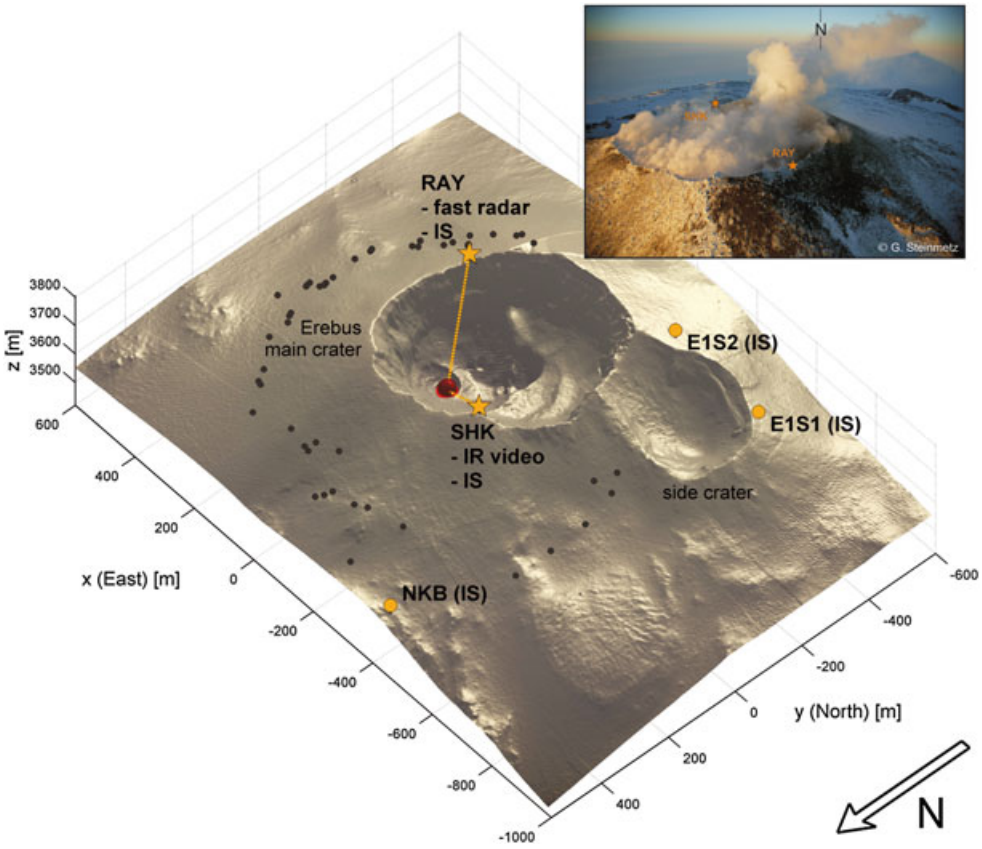

Figure 3. *Digital elevation model of Mt. Erebus summit region*. Data acquisition sites are shown as orange stars (crater rim location) and circles (no line of sight to lava lake). Black dots indicate positions of the farthest flying fresh bombs that were found during the 2005–2006 field season (provided by N. Dunbar, see *Gerst et al.* [2008]). DEM provided by *Csatho et al.* [2005]. The inlay shows an aerial view of the crater region from the austral summer 2005/2006, with radar acquisition sites indicated (provided by G. Steinmetz).

distances as close as a few hundred meters. During larger explosions (Figure 2 top), the partially solidified surface of the ∼40 m diameter lava lake rapidly (∼0.4 s) expands in a geometrically simple manner before violently disintegrating into lava bombs that are frequently ejected over 600 m from the vent. Those eruptions are more energetic than the ones described by *Gurioli et al.* [2008] for a somewhat similar setting at Villarrica Volcano, Chile. Most of the lava bombs at Erebus fall back into the ∼600m wide main crater (Figure 3).

[6] A newly developed high-speed frequency modulated continuous wave (FMCW) Doppler radar (type MVR4; for technical information, see *Vöge and Hort* [2009]; *Hort and Seyfried* [1998]; and *Gerst et al.* [2008]) was deployed on the crater rim at a distance of ∼300 m from the lake to determine the velocity of the expanding magma shell and subsequent ejecta (Figure 3). A network of infrasonic broad band microphones was present (*Jones et al.* [2008]; *Aster et al.* [2004a], see also technical specifications in section A1), and a video camera sensitive in the visible and partly in the infrared spectrum was deployed on the crater rim [*Aster et al.*, 2004a]. In addition to the relatively new observational instrumentation summarized above, persistent activity of Erebus volcano has been monitored since the 1970s with seismic instrumentation. We utilize the most recently installed digital seismic network [*Aster et al.*, 2004a], which comprises a mixture of broadband Guralp 40 T (30 s period) and short-period seismometers. Using this multiparameter network, 55 jointly recorded explosions were observed between 15 Dec 2005 and 2 Jan 2006. Full details of the seismic system are summarized by *Aster et al.* [2004a], and a more detailed description of the full experiment configuration can be found in *Gerst* [2010].

[7] The strategy for this study is as follows: Doppler radar allows for direct velocity measurements of the expanding magma shell surface at a high sampling rate. We will first derive a detailed geometrical model of an expanding magma shell above a gas pocket. The model is chosen such that its main parameter can be constrained by radar measurements. We will then use the geometrical parameters of the magma shell to derive its individual energy terms as a function of its expansion speed (which can be measured by radar) and finally relate these to the overall energy balance of the expanding gas underneath the shell. This allows us to determine a variety of physical explosion parameters by measuring the shell expansion speed with radar.

[8] Within the context of our model, we examine the data set and characterize different explosion types. One set of explosion types is especially amenable to deriving the overpressure in the gas prior to its burst and is used for

calculating synthetic infrasound signals. Finally, a full energy balance for the first ∼1 s of a bubble burst explosion is presented.

2. Theory

2.1. Energy Balance

[9] The driving force behind strombolian explosions is the energy stored in hot and pressurized gas within a buoyantly rising gas pocket (i.e., the gas internal energy). This energy is transferred to all dynamic types of energy that are involved in the bubble's final rapid expansion and explosion. The laws of thermodynamics state that this energy must be conserved. For the initial phase of the explosion, we consider six energy terms:

$$W_{\text{gas}}(t) = E_{\text{total}}(t) = E_{\text{kin}}(t) + E_{\text{pot}}(t) + E_{\text{diss}}(t) + E_{\text{surf}}(t) + E_{\text{atm}}(t) + E_{\text{seis}}(t), \quad (1)$$

where W_{gas} is the gas' internal energy and E_{kin}, E_{pot}, E_{diss}, E_{surf}, E_{atm}, and E_{seis} refer to the explosion's resulting kinetic, potential, viscously dissipated, surface, infrasonic, and seismic energies, respectively (see Notation table). These energy terms describe a short-term energy budget for explosions, and do not include the steady-state heat and gas output *between* explosions [e.g., *McGetchin and Chouet*, 1979]. An additional important, but somewhat separate, energy term is the magma's thermal energy contained in the bubble shell. This type of energy is passively carried by the hot ejecta rather than transported by the gas bubble. Since radiative and convective cooling processes are negligible within the sub second time frame of the onset of an explosion, the magma's thermal energy can be considered as constant during this time, and therefore does not appear in the above equation (note that the gas thermal energy is included in the equation through the gas internal energy term). As will be shown, although magmatic thermal energy does not appear in (1), it must be included when calculating the long-term energy output of an explosion, since it is by far the largest energy transport mechanism when considering time scales longer than that of the first moments of an explosion.

[10] Differentiating (1) with respect to time yields the total power output at time t during an explosion:

$$P_{\text{total}}(t) = P_{\text{kin}}(t) + P_{\text{pot}}(t) + P_{\text{diss}}(t) + P_{\text{surf}}(t) + P_{\text{atm}}(t) + P_{\text{seis}}(t). \quad (2)$$

Since all powers involved in this process are functions of time, a time-varying mathematical description of the expanding gas slug and the bulging of the lava lake surface is necessary to calculate these energies.

2.2. Geometrical Model of an Expanding Magma Shell

[11] We assume that at the time just before initial movement of the lava lake surface, the material between the approaching hot magmatic gas slug (with a pressure p) and the lake surface can be approximated by a circular magma disk, or shell, of thickness h_0, where h_0 is much smaller than the lake radius R_L (Figure 2 bottom). The evolving shape of this shell is represented as a section of the surface of a sphere of variable dimensions, with the boundary condition that there is no movement at the edges of the lake (i.e., the lake shore is a "hinge"). This shell is thus pushed up and flexed outward by the gas pressure as a round shell that is attached to the edge of the lake (Figure 2 bottom and Movie S3 in the supporting information).

[12] The total magma shell mass m_m and therefore its magma volume V_m is assumed to be constant during the rapid acceleration and expansion phase of the explosion, because once this phase has started, the lateral loss of material from the shell is negligible due to magma viscosity hindering drainage. The volume spanned by the doming shell, V_{cap}, is assumed to enclose hot magmatic gas from the top of the rising slug. During the expansion phase, the shell expands its area while thinning to preserve its total mass and magma volume. The absolute position and shape of the shell with time, given the above geometric constraints, can be described with the single parameter $H(t)$ representing the height of the shell zenith point above the initial undisturbed lake level (Figures 2 bottom and A1 in section A2).

[13] We consider this model geometry to be a good representation of Erebus explosions based on video observations of numerous explosions (see Figures 2 and 6 below, or videos in the supporting information). It also fits observed geometries of expanding and bursting bubbles on smaller scales, such as in laboratory experiments, [e.g., by *James et al.*, 2004, Figure 6b], and observations of volcanic mud bubbles.

[14] In addition to H, the only significant parameters that influence the model are the lake radius and the total shell mass, both of which can be estimated by an observer on the crater rim [*Dibble et al.*, 2008] and can further be constrained by examining ejecta sizes. To apply this model to our observations, we need to describe the model as a function of the time-variable magma shell zenith position H, and then determine $H(t)$ from radar data.

[15] To define the surface position $\vec{r}$ of the expanding bubble as a function of H, we fix our coordinate system origin in the center of the undisturbed circular lava lake (Figure A3 in section A2) and introduce the auxiliary parameter q (where $q \in [0 \ldots 1]$; it will later be eliminated, see section A2). Due to the cylindrical symmetry around the vertical axis, we can describe $\vec{r}$ in the (x, z)-plane (which is the vertical plane that includes the lake center as well as the radar device) using two-component vectors, i.e., describing a cross section of the bubble in that plane. This greatly simplifies subsequent analytical solutions for all energy terms. In section A2, we find

$$\vec{r}(q) = \begin{pmatrix} r_x \\ r_z \end{pmatrix} = \begin{pmatrix} \sqrt{qH^2(1-q) + qR_L^2} \\ H(1-q) \end{pmatrix}, \quad (3)$$

and its time derivative $\dot{\vec{r}}(q)$, giving the surface velocity of the shell at point $\vec{r}(q)$:

$$\dot{\vec{r}}(q) = \begin{pmatrix} \frac{qH\dot{H}(1-q)}{\sqrt{qH^2(1-q)+qR_L^2}} \\ \dot{H}(1-q) \end{pmatrix}. \quad (4)$$

Since the surface velocity can be measured by radar, these relatively simple relations will allow us to analytically describe the model's fundamental physical parameters, such as the different kinds of energies of the magma shell as a function of H. Thus, we can constrain the model through determination of H derived from radar observations.

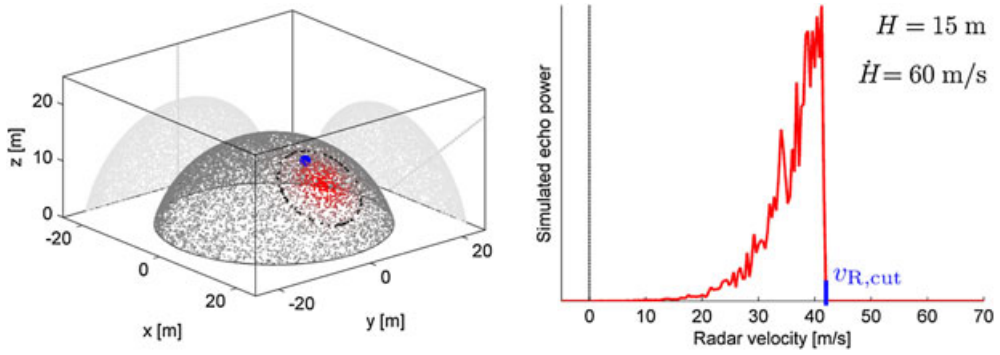

Figure 4. Simulated velocity spectrum of an expanding bubble representing Erebus geometry. (left) Surface of a 15 m high bubble, expanding with a zenith velocity of 60 m/s, approximated by randomly located surface reflectors (dots). The red area is illuminated by the radar beam, fading away from the beam center according to the antenna gain pattern (black line marks –10 dB). The blue dot is the point on the bubble surface that is moving fastest toward the radar. (right) Corresponding simulated radar spectrum, as would be recorded by a radar on the crater rim. A typical feature is the distinct cutoff velocity $v_{R,cut}$ on the right side of the spectrum, caused by the bubble's curved surface. It indicates the radar velocity of the blue dot at left.

2.3. Model Constraints From Radar Observations

[16] To connect radar observations to the geometrical model described above and, ultimately, to the energy terms in (1), it is necessary to describe the movement of the cap in its native parameters $H(t)$, $\dot{H}(t)$, and $\ddot{H}(t)$, in terms of the measured radar velocities. A Doppler radar only measures the velocity component of the observed object that is along the radar line-of-sight, i.e., the beam-parallel velocity component or radar velocity. Moreover, our observations do not describe a single object in the radar beam, but instead include all surface points on the magma cap that are within the beam, summing up all of their echoes in a velocity spectrum (Figure 4).

[17] Figure 4 (right) shows the simulation of such a velocity spectrum at an arbitrary time during an assumed bubble expansion. This was achieved by simulating 10,000 random reflectors on the surface of the bubble (Figure 4 left, gray dots), with a zenith expansion velocity of $\dot{H} = 60$ m/s. Every moving reflector has a certain velocity component in the radar line-of-sight direction, and a cross section that depends on its line-of-sight surface area. Summing up the contributions of reflectors within the radar beam (red dots) leads to a velocity spectrum (right) at that specific time.

[18] Figure 4 is representative of the experiment geometry at Erebus, illustrating that a single radar spectrum incorporates information about a significant area of the bubble surface. It is therefore generally difficult to attribute a single observed feature in the radar velocity spectrum (e.g., a peak at a certain velocity) to its respective surface point on the magma cap. Yet, a useful and easily determined feature of the spectrum is the abrupt cutoff of echo power at maximum velocity (Figure 4). For a uniformly expanding shell, the peak just before the cutoff represents the radar velocity of the surface region that is moving fastest toward the radar (blue dot). This distinctive *cutoff velocity* ($v_{R,cut}$) is equal to the *maximum velocity* of the spectrum (i.e., the maximum velocity at which there is significant echo power), as long as the object in the radar beam is an intact bubble surface. It can both be easily identified in a spectrum and also be attributed to a unique point on the cap surface, i.e., the point on the surface that moves fastest toward the radar. Therefore, calculating the velocity of this point in the bubble model as a function of H will provide the necessary relation between model and radar data (section A2), where

$$\dot{H}(t) = \frac{v_{R,cut}(t)}{\max\limits_{q \in q_0, q_1} \left(Q(q, H(t)) \right)}. \tag{5}$$

Together with (3) and (4), we can now establish a direct relation between physical parameters of the magma shell (H,$\dot{H}$) and measured radar velocities ($v_{R,cut}$). Thus, H and $\dot{H}$ can now be determined for every point of time during the explosion prior to shell burst.

2.4. Energy Calculations From Measured Quantities

[19] Within the geometrical model established above, we can calculate the energy terms in (1). Using (3) and (4), each term is a function of parameters that can be directly determined by radar (i.e., bubble zenith height H, as derived from radar cutoff velocities), and of model parameters that can be otherwise reliably estimated (e.g., lake radius R_L and magma shell mass m_m). Detailed derivation of all equations can be found in *Gerst* [2010].

2.4.1. Pressure-Volume Work

[20] For *adiabatic processes* the differential amount of pressure-volume work is given by

$$\mathrm{d}W_{gas} = p_{gas}\, \mathrm{d}V_{gas}. \tag{6}$$

Here p_{gas} is the current gas overpressure inside the bubble (i.e., in excess of the surrounding atmospheric pressure, which is ~625 hPa at Erebus). V_{gas} is the total gas volume in the bubble (i.e., contained inside the cap and the slug tail). We treat the final rapid expansion of the gas bubble as adiabatic, assuming a negligible heat transfer from magma into the gas during the subsecond time frame of an explosion.

[21] Since the slug tail can be considered static within the time frame of an explosion, the time derivative, $\dot{V}_{gas}$ can be

reduced to $\dot{V}_{\text{cap}}$ (equation (A10); section A2), giving

$$\dot{W}_{\text{gas}} = p_{\text{gas}} \dot{V}_{\text{cap}} = \frac{\pi}{2} p_{\text{gas}} \dot{H} \left(H^2 + R_L^2\right), \quad (7)$$

where $\dot{W}_{\text{gas}}$ can be determined from (1). This describes the relation between the underlying gas pressure, gas volume, and the power output of an explosion. Therefore, when the volume expansion and the energy output are measured (e.g., via radar observations), the gas pressure during the explosion can be calculated.

2.4.2. Kinetic Energy of the Magma Shell

[22] The kinetic energy of the expanding shell is

$$E_{\text{kin}} = \frac{m_m \dot{H}^2}{4H^6} \left(H^2 + R_L^2\right) \left(H^4 - 2R_L^2 H^2 + 2R_L^4 \ln\left[1 + \frac{H^2}{R_L^2}\right]\right), \quad (8)$$

where m_m is the shell mass. This equation is derived from the classical "$E_{\text{kin}} = 1/2\ mv^2$" integrated over the shell volume. During the explosion, kinetic energy is not only stored in the magma shell but also in the outward accelerating gas inside the bubble. However, since the overall mass of this accelerated magmatic gas is about 3 orders of magnitude smaller than the mass of the magma shell, its preburst kinetic energy is negligible [e.g., *McGetchin and Chouet*, 1979] in comparison to the kinetic energy of the shell.

2.4.3. Potential Energy of the Magma Shell

[23] The potential energy of the magma shell, lifted in Earth's gravity field, is found by integrating gravitational force over the vertically raised volume. For a spherically expanding shell, this gives

$$E_{\text{pot}} = m_m g \frac{H}{2}. \quad (9)$$

2.4.4. Energy Dissipated Through Viscous Flow Inside Shell

[24] A Newtonian rheology was assumed, even though this is not always a valid approximation for rapidly straining magma [e.g., *Webb and Dingwell*, 1990; *Dingwell et al.*, 1993; *Divoux et al.*, 2008]. However, we consider it to be a sufficient approximation for this task [see also *James et al.*, 2004], and the amount of viscously dissipated energy is small compared to the total amount of energy released during an explosion (Figure 11 below). We obtain

$$\dot{E}_{\text{diss}} = \frac{12 \mu_m V_m H^2 \dot{H}^2}{\left(H^2 + R_L^2\right)^2}. \quad (10)$$

2.4.5. Shell Surface Expansion Energy

[25] Preeruptive expansion energy E_{surf} is consumed by the surface area expansion of the shell

$$\dot{E}_{\text{surf}} = 4\pi \sigma_m H \dot{H}, \quad (11)$$

where σ_m is the specific surface energy. Following *Walker and Mullins Jr* [1981] and *Koopmann* [2004], we use σ_m = 0.4 N/m, a value that has been commonly utilized [e.g., *Vergniolle and Brandeis*, 1994].

2.4.6. Acoustic Energy Radiated Into the Atmosphere

[26] Assuming that at the frequencies of interest (<1 Hz), the expanding bubble surface can be described as an acoustic monopole [*Lighthill*, 1978] and we obtain

$$\dot{E}_{\text{atm}} = \frac{\pi \rho_a}{8 c_a} \left(2H\dot{H}^2 + \ddot{H}\left(H^2 + R_L^2\right)\right)^2 + \frac{\pi \rho_a}{8 R_L} \dot{H}\left(H^2 + R_L^2\right)\left(2H\dot{H}^2 + \ddot{H}\left(H^2 + R_L^2\right)\right). \quad (12)$$

The second of the two terms refers to the energy that is temporally stored in the near field. Both terms contribute in roughly the same order of magnitude to the sound power output. The equations show that it mainly increases with the second derivative of the volume of the cap. Because the cap volume increases with the third power of the cap zenith height (A5), the most effective sound power output is expected late in the explosion, where the bubble shell has acquired a considerable size.

2.4.7. Ground Reaction Force and Seismic Energy

[27] Radiated seismic energy estimation presents perhaps the most difficult calculation for the energy budget due to the complex structure of the volcano, which is associated with a complex force coupling mechanism into the surrounding rock. Instead of modeling this in detail, which would require the introduction of numerous unconstrained assumptions, we treat the seismic source zone as a black box that must adhere to Newton's Second Law, i.e., forces that vertically accelerate a magma cap upward must act as a downward reaction force on the ground in exactly the same strength. Therefore, this approach does not consider second-order effects, such as the complex interaction between the falling magma film around the base of the slug and the surrounding rock [*Lane and Gilbert*, 2008].

[28] This vertical ground reaction force provides the input for all our seismic calculations and can be readily calculated from Newton's Second Law using (A16) and (4). It is given by the sum of the acceleration forces exerted by each mass element, i.e., by the acceleration force density integrated over the whole volume of the shell

$$F_{\text{ground},z} \approx -\int_M \ddot{r}_z(\vec{r})\, \mathrm{d}m = -\frac{1}{2} m_m \ddot{H}(t), \quad (13)$$

where $\ddot{r}_z$ is the magma shell material's vertical acceleration.

[29] The equation does not take into account any shell fragments falling back into the crater pit in the seconds after the explosion, since their influence can be expected to be much smaller (spread out) than the initial force impulse. Considering body waves radiated into an elastic half space [*Haskell*, 1964]

$$E_{\text{seis}} = \left(\frac{1}{6\pi \rho_{\text{rock}} v_p^3} + \frac{1}{3\pi \rho_{\text{rock}} v_s^3}\right) \frac{m_m^2}{4} \int_{-\infty}^{\infty} \dddot{H}^2\, dt, \quad (14)$$

where v_p and v_s are compressional and shear velocities and ρ_{rock} is the density of the half space. For a Poisson's ratio near 0.25 ($v_p/v_s = \sqrt{3}$), (14) predicts that approximately 95% of the far-field seismic energy from this simple source model will be radiated as *S* waves.

[30] A shortcoming of (14) is that it assumes no generation of Rayleigh waves, which is clearly inaccurate for a near-surface source and a simple elastic medium. However, observations on Erebus volcano with dense short-period seismic networks (see below) indicate that the seismic wavefield that is emerging from Erebus explosions very rapidly spreads and predominantly equipartitions into a highly scattered *S* wavefield. This is due to the strong seismic heterogeneity and topography of the volcano summit region [*Chaput et al.*, 2012]. We consider the use of (14) and other modeling of the seismic wavefield in greater detail below.

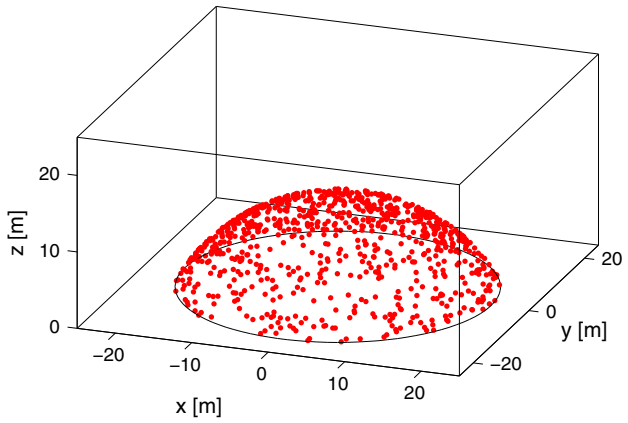

Figure 5. Approximating a noncompact sound source by superposition of randomly distributed compact monopole sources (red dots). The strength of each of the sources at a given time depends on their current acceleration on the expanding surface.

2.4.8. Thermal Energy of Magma

[31] While the magma's thermal energy term due to the lack of significant heat exchange in the time frame of an explosion is not included in (1), we quantify it separately here to demonstrate its magnitude in relation to the dynamic energies. We find

$$\Delta E_{\text{therm}} = m_m \, c_{p,m} \, \Delta T, \tag{15}$$

where $c_{p,m}$ is the specific heat of magma, not taking into account any effects arising from changes in the crystal content during the cooling. An approximate value used here is $c_{p,m} \sim 1000$ J/kg/K [e.g., *Jaeger*, 1964; *Calkins et al.*, 2008] and $\Delta T \sim 1000$ K.

[32] In addition to the heat stored in the magma mass, a small amount of thermal energy is also liberated from hot magmatic gas during an explosion. However, when compared to the energy stored in the heavy magma shell, this contribution is negligible [e.g., *McGetchin and Chouet*, 1979].

2.5. Infrasonic Signals From Expanding Surface Bubbles

[33] Although (12) allows for the calculation of the overall acoustic power released during a lava lake explosion, we determine the detailed infrasonic signal through considering the finite (i.e., non-compact) distribution of acoustic point sources. We therefore computed the expected acoustic signal of an explosion at an observer's position through a *Green's function* solution assuming a large number of small sound sources distributed over the surface of the lava lake [*Stepanishen*, 1998; *Ehrenfried*, 2003].

[34] As shown in Figure 5, we generated random points on the surface of the expanding lava lake. These points represent small compact monopole sources of sound, and their combined phase and strength add up to the total generated infrasound signal observed at a defined point at distance. Their number N_{sources} was chosen in each time step so that the average surface area of each source is 2 m^2 (i.e., more than 1000 points on the surface).

[35] To calculate the strength of each source, the acceleration of each surface point ($\ddot{\vec{r}}_n(q, \Phi, t)$) was calculated from (4), which, when multiplied with the unit normal vector ($\hat{\vec{n}}_n(q, \Phi, t)$), yields the volume acceleration of each source (effectively adding up to the overall volume acceleration $\ddot{V}_n$ of the gas underneath the shell):

$$\ddot{V}_n(q, \Phi, t) = \frac{A_{\text{cap}}}{N_{\text{sources}}} \, \ddot{\vec{r}}_n(q, \Phi, t) \cdot \hat{\vec{n}}_n(q, \Phi, t), \tag{16}$$

where A_{cap} is the surface of the shell cap (A6). The source's individual pressure signal p_n created in a half-space at the position of an observer or a microphone at distance $r_{\text{mic,n}}$ is then given by [*Lighthill*, 1978]

$$p_n(q, \Phi, t, r_{\text{mic,n}}) = \frac{\rho_a}{2\pi r_{\text{mic,n}}} \, \ddot{V}_n \left(q, \Phi, t - \tfrac{r_{\text{mic,n}}}{c}\right). \tag{17}$$

$r_{\text{mic,n}}$ is not only a function of the observer's distance and elevation angle but also a function of q, Φ, and t. Therefore, it has to be determined individually for each source point. The sum of all source signals represents the total pressure signal p_{mic}, expected at a microphone at distance r_{mic} from the lava lake center at an elevation angle of ϕ_{mic}:

$$p_{\text{mic}}(r_{\text{mic}}, \phi_{\text{mic}}, t) = \sum_n p_n\left(q, \Phi, t, r_{\text{mic,n}}\right). \tag{18}$$

Since every p_n is a function of H, this pressure can be determined from radar data (5).

3. Observations

[36] We utilize data from a fast MVR4 Doppler radar device operating at location RAY as well as data from a video camera at location SHK, i.e., both installed on the crater rim with near-orthogonal lines of sight (Figure 3). Additionally, we describe infrasonic waveform recordings that will be used in the interpretation of results.

3.1. Thermal Video

[37] The video camera installed at the crater rim [*Aster et al.*, 2004a] was sensitive in the visual as well as in the thermal spectrum and allowed for the visual observation of explosions. Weather and volcanic plume conditions limited video observation to only about half the explosions that were observed by radar. A characteristic snapshot of each of the visually observed explosions is shown in Figure 6. A selection of video files is available in the supporting information.

[38] Explosions at Erebus were classified into four different types: I, II, *small*, and *blurred*, according to their explosion characteristics. Types I and II are by far the most frequent and can be categorized as the "standard" type explosions observed at Erebus during the observation period. While these two principal explosion types both affect the whole surface of the lava lake, they are characterized by differing surface acceleration behavior. For more details on these four explosion types the reader is referred to *Gerst* [2010].

[39] Type I (Movie S1) explosions typically display an accelerating bulging of the complete lava lake surface prior to bursting. Type II explosions, in contrast, initiate via violent puncturing of a small area of the lake surface without significant prior surface expansion (Movie S2).

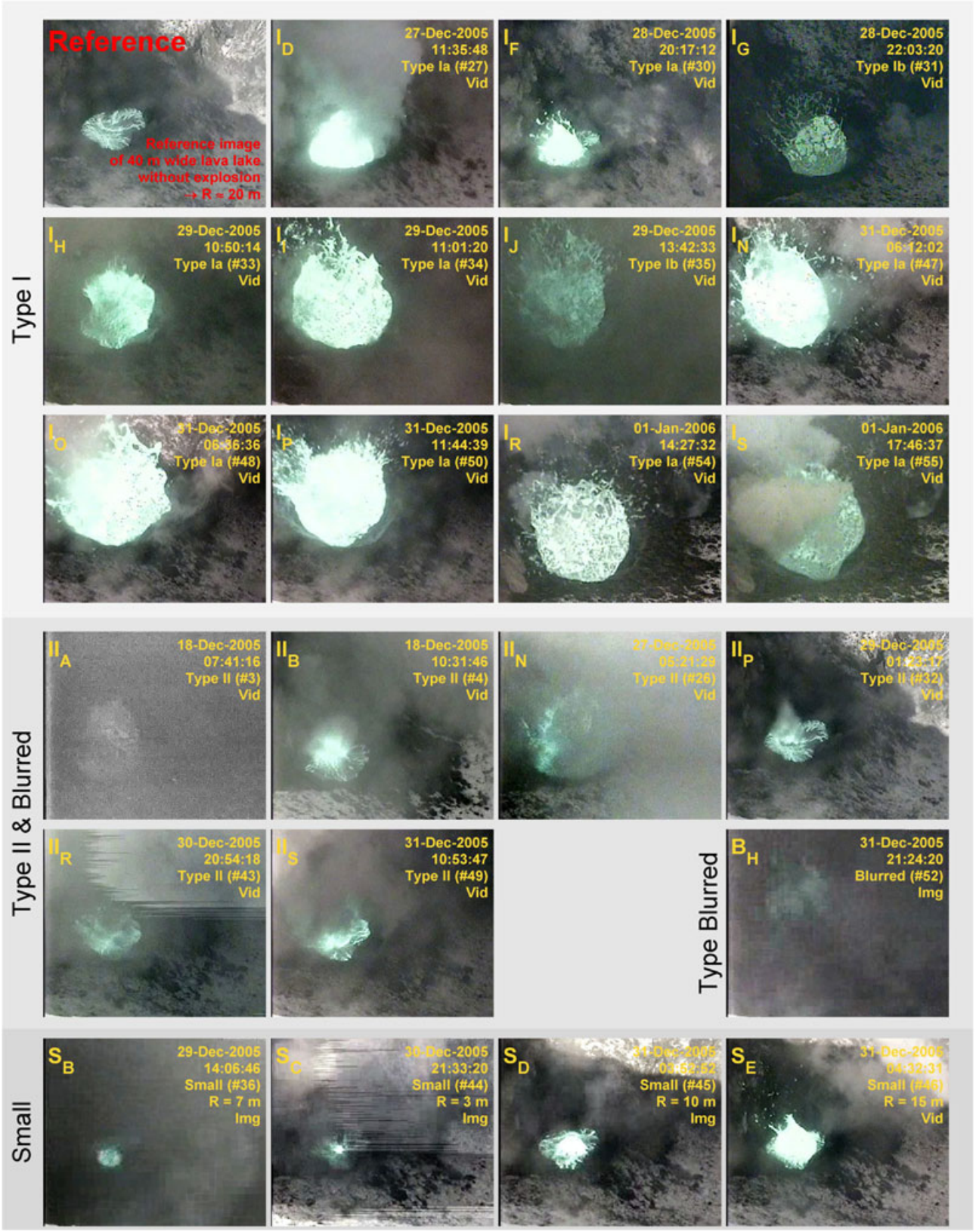

Figure 6. Thermal video snapshots of explosions that were observed both by radar and by thermal camera (weather permitting). "Hot" pixels are shown in green. The unique identifier for each explosion includes the explosion type for each event (I, II, *S*/*small*, and *B*/*blurred*). Where stated, *R* denotes the approximate radius of the affected region of the lake surface (where *R* is not noted, the entire surface was affected). For video files, see supporting information and *Gerst* [2010].

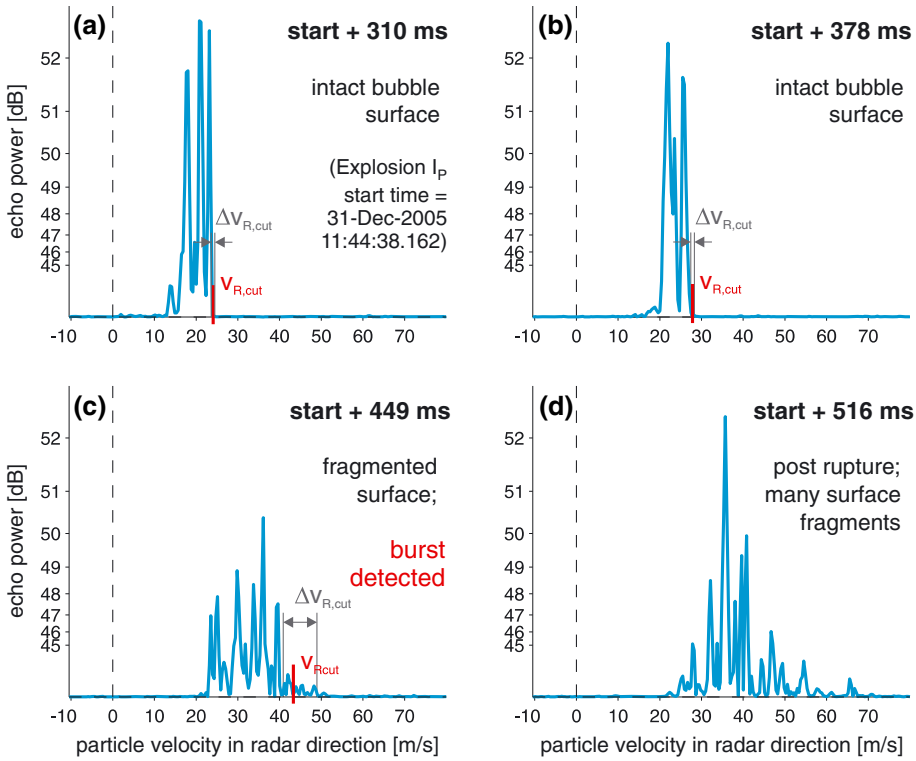

Figure 7. *Example series of spectra of a typical type I explosion (I_P)*. Burst time is identified as the moment when the bubble's radar echo spectrum transits from (a and b) narrow (as expected, see Figure 4) to (c and d) a wider spectrum reflecting many bubble surface fragments in the radar beam.

Video observations suggest that these two explosion types have a similar underlying mechanism of gas slug delivery, but that type II explosions show an early expansion asymmetry that leads to early rupture of the lava lake surface, probably due to the development of a fast rise path due to localized lake crust thinning in the lava lake convection system. Video data for both these types of explosion show that in the ~10 s before the rapid expansion phase, the lava lake level typically rises by a few meters, with an acceleration toward the end. They also show that types I and II explosions typically affect the entire surface of the lava lake in accordance with our expansion model.

[40] *Small* explosions, as the name suggests, resemble smaller and lower energy examples of types I and II and typically occur as small bubbles that do not affect the whole surface of the lake. Finally, *blurred* explosions refer to their appearance in the radar velocity spectra, where they have a somewhat fuzzy shape that prevents the picking of cutoff velocities. Visually, *blurred* explosions are very similar to types I and II explosions and might simply be a subgroup of them in which an unfavorable observation geometry leads to a blurring of the radar spectra.

[41] While types I and II explosions are equal in number (19 each), only six *small* and eight *blurred* explosions were detected. During three explosions, the radar data had data gaps that did not allow for the sampling of cutoff velocities.

3.2. Radar Velocity Spectra

[42] Our Doppler radar measured velocity spectra of explosion ejecta (Figure 7) at a rate of ~14 spectra per second at a line-of-sight distance of 315 m to the lake center, with an observation angle of 39° to the horizontal. The radar's field of view was 3° at –10 dB (Figure 4).

[43] We use the measured Doppler radar spectra (Figure 7) to pick *radar cutoff velocities* ($v_{R,cut}$, see (A22)), which allow to calculate a bubble's surface velocity when applying the bubble expansion model. Figure 8 shows radar velocity spectra for all measured explosions of type I as so called *velocigrams*. Instead of showing single radar spectra (as in Figure 7), this type of illustration allows visualization of a time series of several velocity spectra in one plot, where echo power is translated into a color map, and radar velocity is shown on the vertical axis. Therefore, brightly colored areas in the velocigram allow us to follow the temporal development of velocities in the radar beam.

[44] We typically observe that, at the moment of shell burst, the radar signature changes from a single expanding surface to that of multiple fragments in the radar beam moving at various speeds (Figure 7). Smaller fragments show an acceleration at that time, while larger shell fragments stop accelerating. This is most likely due to the pressurized gas escaping through cracks in the bubble shell at burst time, further accelerating small fragments while large ejecta, due to their inertia combined with rapidly falling gas pressure, do not further accelerate. This effect is characterized by a spread in the velocity spectrum (Figure 7c; shown as stars in Figure 8) and allows us to determine the time of shell burst through radar data (verified by video). After the burst, the shell ceases to exist as a single body, and due to the spread in the spectra, cutoff velocities can no longer be picked. Therefore, for further processing (e.g., for applying the bubble expansion model), only the preburst spectra were used.

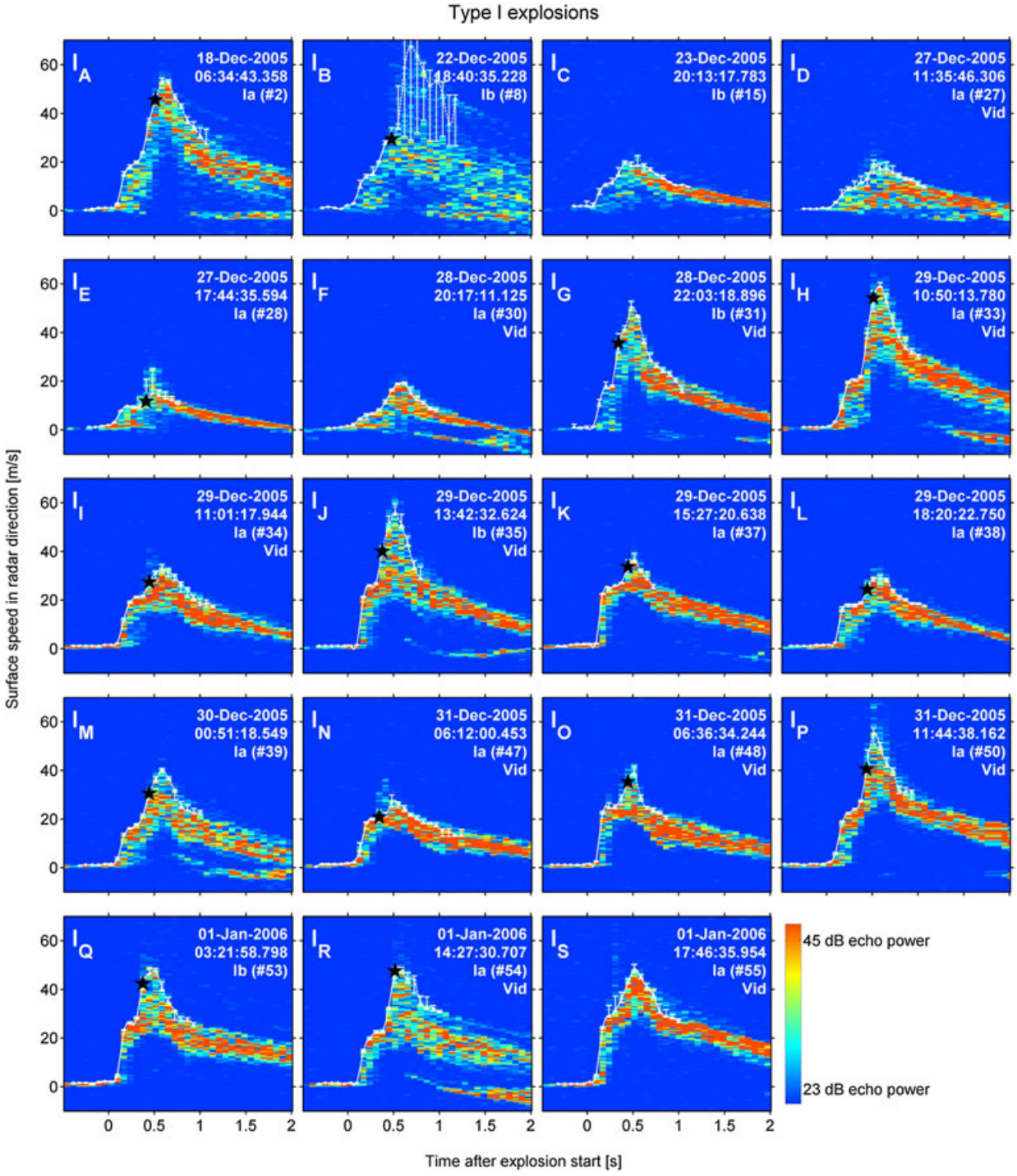

Figure 8. Radar velocigrams of type I explosions. The text annotation shows the origin of the time axis (= explosion start time) and the explosion type. Explosions for which a thermal video is available are marked with "Vid." The color bar shows the echo power in dB (scale is nonlinear). White contours show the picked cutoff velocity and its error range for each spectrum, black stars mark the burst times.

[45] To quantitatively propagate pick quality into subsequent calculations, error ranges $\Delta v_{R,cut}$ were introduced for each spectrum (Figure 7; white bars in Figure 8). Error ranges were manually picked from single spectra with the aim of including the true cutoff velocity with at least 95% likelihood. Consequently, the width of the error range is relatively large when the spectrum consists of a broad group of peaks (e.g., after burst time), and is as small as the sample width of the velocity axis (i.e., the velocity resolution, in this case 0.39 m/s) when the cutoff is very sharp. The pick of $v_{R,cut}$ is not necessarily in the center of the error range because of the asymmetrical shape of the falling upper flank in the spectrum.

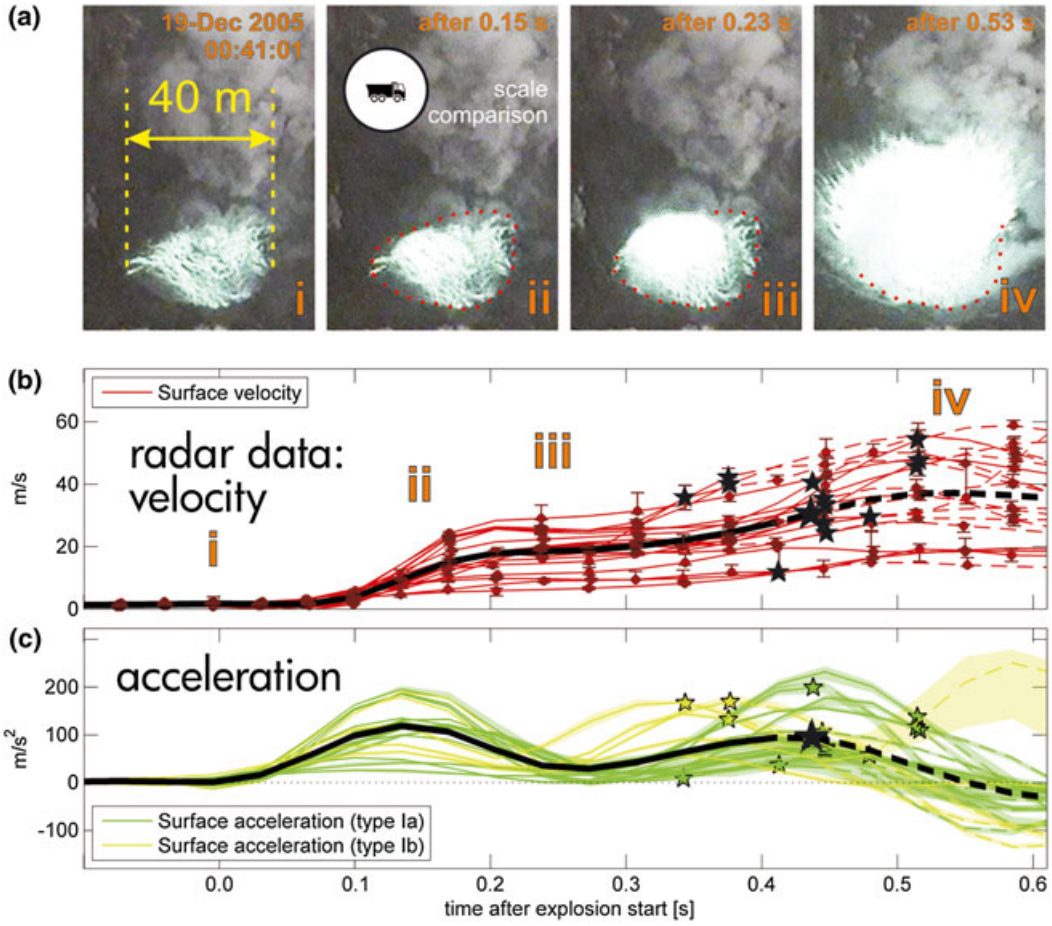

Figure 9. Radar data. (a) Video sequence for time comparison (repeated from Figure 2) (b) Bubble surface velocities for type I explosions measured with Doppler radar. Stars annotate times when bubble shell burst is detected by radar, after which the shell fragments into bombs (dashed lines). Black curve shows the trace mean, and velocity uncertainties are indicated by error bars. (c) Bubble surface acceleration for type I explosions measured by radar, typically showing two acceleration peaks during explosions. According to the time between these peaks, explosions were grouped into types Ia (∼0.3 s, dark green) and Ib (∼0.2 s, light green) for better comparison. Underlying shades show the standard error resulting from propagation of picking and parameter uncertainties.

[46] Figure 9 (red traces) shows the same cutoff velocity traces that were already shown as white lines in Figure 8, but plotted into a single figure summarizing several explosions. Velocity curves were transferred into displacement and acceleration by numerically integrating and differentiating, respectively. All explosions have in common that shortly after their start, the surface velocity of the bubble strongly increases, leading to a rapid acceleration and strong relative expansion of the shell. This phase, which typically ends after 0.2–0.3 s for types I and II explosions, will be referred to as the *rapid expansion phase* of an explosion (see Movie S3).

4. Application of the Bubble Expansion Model

[47] We will concentrate on the highly repeatable and symmetrical type I explosions, which are not influenced by the complications discussed above. Type I explosions can be characterized by four stages (Figure 9a). (i) An undisturbed lava lake surface, (ii) doming of the lake surface, (iii) upward expansion of the entire lake surface, and (iv) bursting of the lava shell, after which bomb fragments travel independently on ballistic trajectories accompanied by the atmospheric expansion of a previously contained slug gas.

[48] Some type I explosions reach bubble surface velocities of up to 60 m/s before bursting (Figures 9b and 10b). After burst, a subset of smaller ejecta is typically further accelerated by the escaping gas, exceeding 150 m/s during large type II explosions [*Gerst*, 2010, p. 116].

[49] Interestingly, shell accelerations do not show a straightforward single maximum in time as might be expected (and which is observed for type II explosions). Instead, type I explosions typically show two distinct acceleration peaks separated by roughly a third of a second (Figure 9C; Movie S3), with the magma shell burst typically occurring during the second peak.

[50] It should be noted that despite the above mentioned peaks, measured accelerations are always positive, i.e., the shell material is moving away from the explosion center at all times during the explosion with an increasing speed. This rules out models that attempt to explain infrasound signals from such explosions proposing several oscillations of the

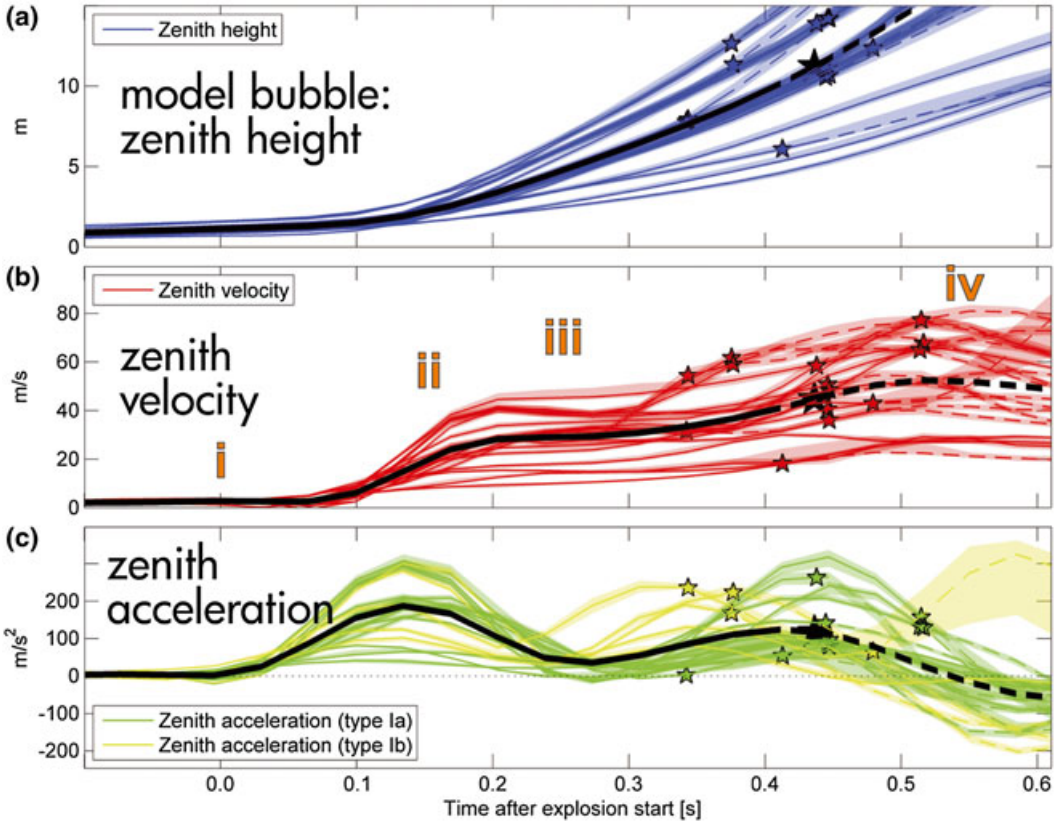

Figure 10. *Model bubble parameters* for type I explosions, obtained by geometrically translating the radar data shown in Figure 9 into parameters of our bubble model (Figure 2). The curves refer to the bubble's zenith point, which is vertically moving away from the undisturbed lake center. (a) Zenith height H above initial lake level at beginning of explosion. Annotations are similar to Figure 9. (b) Bubble zenith velocity $\dot{H}$. (c) Zenith acceleration $\ddot{H}$. Note the overall shape similarity with Figure 9, which reflects that the model bubble parameters are merely geometrical corrections to the initial motion parameters that were obliquely measured by radar.

intact bubble surface around an equilibrium radius [i.e., with a bubble surface that is moving inward at times; *Vergniolle and Brandeis*, 1994; *Vergniolle et al.*, 1996].

[51] To apply our geometrical bubble model, we geometrically translated the velocities measured by radar into parameters of the bubble model, which are mainly the position and motion of the bubble's zenith point H (Figure 10). This allows us to calculate further bubble parameters of interest, such as energies and gas pressures.

[52] *Gerst et al.* [2008], consistent with our video observations, have demonstrated that bubbles do not always expand symmetrically, but can show slight directivity effects. Since the radar data in this study comes from a single high-speed instrument, we cannot resolve such directivity effects, which means that individual measurements (e.g., expansion speed or burst time) might be somewhat biased in either direction. However, *Gerst et al.* [2008] observe that, while individual explosions can have a lateral expansion velocity component, the average expansion direction is near vertical, i.e., the averaged behavior of several explosions resembles that of a single symmetrical explosion. Thus, in this study, we focus on interpreting the average and common behavior of multiple explosions instead of interpreting single traces.

4.1. Error Analysis and Input Parameters

[53] The bubble expansion model includes multiple nonlinear dependencies, some of which were solved numerically. To obtain reliable information on error propagation, we used a Monte Carlo-style statistical approach where output parameters were computed a large number of times while input parameters were independently randomly varied within their known or presumed error ranges. By comparing the influence of a large number of these randomly varied computations on the output parameters (e.g., energies or pressure), it was possible to determine the influence of known parameter uncertainties on the model results, as well as the general stability of solutions.

[54] All significant model input parameters are shown in Table 1. Most of these parameters were assumed to be normally distributed around their expected values, with a one σ uncertainty range (also shown in Table 1). Picking errors of radar cutoff velocities were also incorporated.

[55] In practice, 10,000 computation runs with randomly varied input parameters produced a quasi-Gaussian set of results for each output parameter. The central 68.3% of this distribution thus approximates a variation of 1 σ around the unvaried result. In the following figures, this 68.3%

Table 1. Model Input Parameters With Uncertainties[a]

Symbol	Name	Expected Value	Estimated 1σ Uncert.	Source	Main Influence On
R_L	Lava lake radius	20 m	± 15%	observation	All output parameters
ϕ_R	Radar elevation angle	39.1°	± 2°	observation	All output parameters
h_{burst}	Shell thickness at burst	0.75 m	± 0.2 m	observation	All output parameters
ρ_m	Density of magma	2000 kg/m^3	± 15%	*Dibble* [1994]	All output parameters
μ_m	Viscosity of magma	5×10^4 Pa s	± 1 magn.	*Sweeney et al.* [2008]	Shell dissipated energy
c_a	Sound speed in air	313 m/s	± 10%	[*Gerst*, 2010, p. 44]	Sonic energy; IS signal
ρ_a	Density of air	0.86 kg/m^3	± 10%	[*Gerst*, 2010, p. 43]	Sonic energy; IS signal
$c_{p,m}$	Heat capacity of magma	1000 J/(kg K)	± 10%	*Jaeger* [1964]	Shell thermal energy
σ_m	Surface energy of magma	0.4 J/m^2	± 25%	*Koopmann* [2004]	Shell surface energy
v_p	*P* wave speed in ground	2200 m/s	± 10%	*Dibble et al.* [1994]	Seismic energy
v_s	*S* wave speed in ground	1270 m/s	± 10%	*Dibble et al.* [1994]	Seismic energy
ρ_{rock}	Surrounding rock density	2400 kg/m^3	± 10%	*Dibble et al.* [1994]	Seismic energy

[a]When entering the model, the above parameters were randomly varied around their expected value, following a Gaussian distribution with a half width equal to the above uncertainty values. Magma viscosity μ_m, due to its wide range, was varied by one order of magnitude in either direction (through a Gaussian distribution of its logarithm).

confidence interval is shown either as error bars or as shaded background color.

4.2. Explosion Energies

[56] Figure 11 shows a time series of all cumulative dynamic energies associated with the first ∼0.6 s of type I explosions, as well as the thermal energy carried by ejecta. The dynamic energy types are, in general order of decreasing magnitude, the kinetic energy of the accelerated magma shell, its potential energy in Earth's gravity field, energy viscously dissipated in the magma shell, infrasonic energy, seismic energy, and energy needed to increase the surface area of the shell.

[57] All dynamic energy types show a similar temporal behavior. Differences between individual explosions reflect their varying strength, as well as possible directivity effects [*Gerst et al.*, 2008], which are not considered here. At the beginning of explosions, energies quickly increase by several orders of magnitude until they tend to level out after around 0.2 s and remain at their current order of magnitude until the shell bursts at around 0.4 to 0.5 s after the explosion start.

[58] The greatest energy by far supplied by the gas pressure is converted to kinetic energy of the shell (∼1 GJ just before burst time) and to its gravitational potential energy (several hundred MJ), making this the controlling factor of all parameters derived from the energy output (e.g., gas pressure and volumes). For typical explosions, they sum to the energy equivalent freed by the explosion of several hundred kg of TNT.

[59] The third largest energy type, significantly smaller than the above, is dissipated energy caused by viscous friction in the magma shell. This energy is converted to heat, therefore raising the temperature of the magma shell while it expands. Yet, even though it typically reaches 10–100 MJ just before burst, it is hardly enough energy to heat the magma shell by more than a few 1000ths of a Kelvin, due to the enormous heat storage capacity (15).

[60] Acoustic energy delivered to the atmosphere is the fourth largest dynamic energy type involved and is typically 1 MJ just before the shell burst. During the phase of rapid expansion of the shell at the beginning of explosions, the acoustic power output briefly exceeds 10 MW (190 dB SWL), which is more than the acoustic power output of large spacecraft-carrying rockets [*Lighthill*, 1978, p. 17].

[61] Seismic energy derived from ground reaction forces is approximately 1 order of magnitude smaller than acoustic energy. At around 50–100 KJ, it amounts to only one 100,000th of the kinetic energy of the shell. Finally, with less than 1 KJ, surface energy stored in the expanding bubble surface is even less significant for the energy budget.

[62] In contrast to the dynamic energies powered by the expanding gas slug, the magmatic thermal energy in explosions is plotted as constant in Figure 11, because it is not freed by the expanding gas bubble, but is instead passively carried by the ∼1000°C hot magma shell and subsequent explosion ejecta. It is on the order of 10^{12} J per explosion, which is equivalent to the energy release of ∼1 kiloton of TNT, therefore exceeding the energy dynamically freed by the expanding gas (10^9 J) by approximately 3 orders of magnitude.

4.3. Slug Overpressures and Gas Volume

[63] The evolution of power output during the rapid shell expansion phase allows for the tracking of gas overpressure within the slug. This is done by resolving (2) and (7) for p_{gas} and summing up all observed energies (8–14). Figure 11b shows derived absolute overpressure values of several explosions during the first acceleration period (0.15–0.25 s; Figure 9c). Gas overpressures during this episode lie between 100 and 600 kPa, (average ∼400 kPa; roughly the pressure in a bicycle tire). During expansion, this pressure rapidly drops to about 100 kPa at the onset of the second acceleration peak, a value within the range of eruptive overpressures previously estimated for Stromboli volcano [*Blackburn et al.*, 1976; *Vergniolle*, 1998; *Ripepe and Marchetti*, 2002] and consistent with recent laboratory modeling [*Lane and Gilbert*, 2008] and theory [*Del Bello et al.*, 2012]. The ∼100 kPa overpressure at burst time is the source of radiated infrasonic energy after the burst.

[64] The gas volume just prior to rapid expansion was estimated using two different methods: (1) assuming adiabatic bubble expansion prior to burst and a specific heat ratio of $C_P/C_V = 1.1$ for hot gas [*Lighthill*, 1978], so that pressure drop time evolution allows the calculation of the gas volume and (2) balancing total released energy

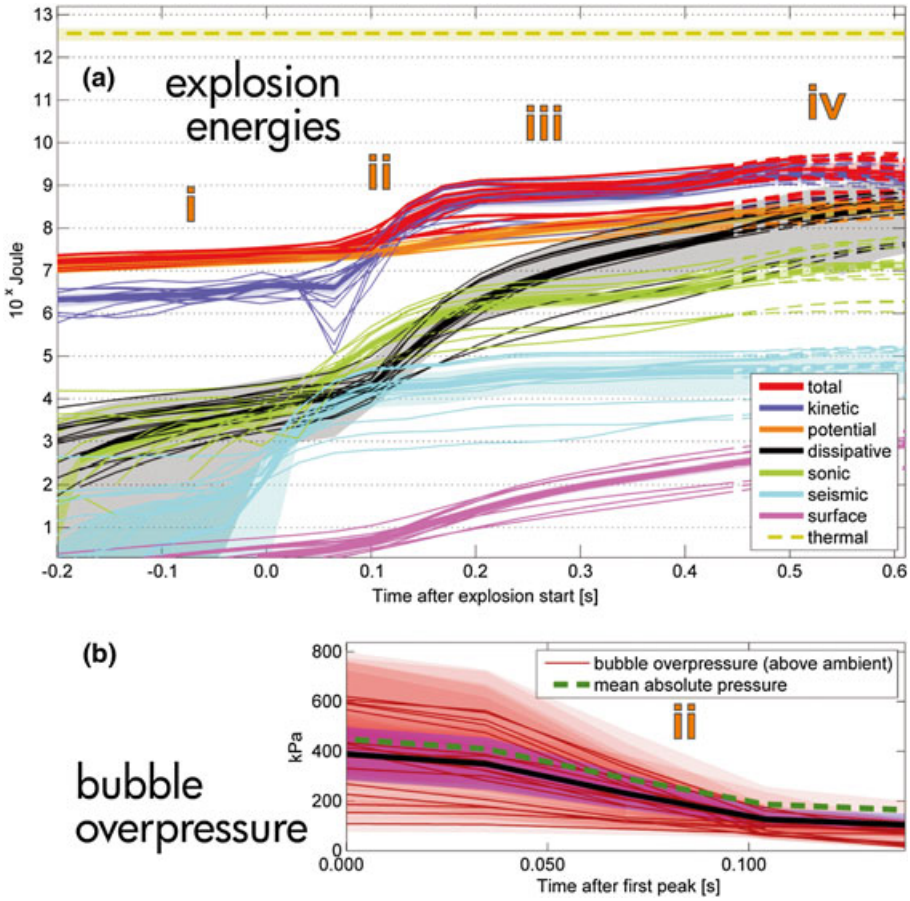

Figure 11. (a) Cumulative plot of explosion energy partitioning with time ($\log_{10}$ vertical axis). Total energy (red) refers to the sum of all dynamic energies (excluding the magma shell's thermal energy, which is shown separately as a dashed yellow line at the top). All lines are dashed after the slug burst and, from that point on, do not represent correct energy values. Bold lines show respective mean traces, with attendant standard deviations shown as shaded regions. Roman numerals refer to explosion episodes (Figure 1). (b) Gas overpressure evolution (above ambient) within slugs during their rapid expansion phase (episode ii) of all type I explosions. Time axis is relative to the first acceleration peak. Individual error ranges are shown as shaded areas in light red, the average error range is shown as a purple-shaded area around the mean. The dashed green line shows the bubble's average *absolute* pressure.

(Figure 11a) with internal gas energy. For most explosions, both methods consistently yield gas volumes (at local T and P inside the bubble just prior to its burst) of 1000–2000 m^3, which additionally are in agreement with independent infrasonic estimates [*Johnson et al.*, 2008], therefore providing a validation point for our model.

[65] The above calculated bubble volume of 1000–2000 m^3 is an order of magnitude less than the size of the post-eruptive void that can typically be observed in clear conditions in videos of the explosions (10,000–30,000 m^3), which is assumed to be a good indicator for the gas bubble volume at burst time (with a small correction for the volume of the ejected magma).

[66] This discrepancy, a stable observation for explosions of various sizes, can be explained by: (1) rapid downward pushing of magma into the conduit during the explosion, as a reactant force to the accelerating shell; or (2) the presence of a secondary slug or complex of bubbles trailing the initial slug, so that the volume estimated from the initial expansion velocity does not reflect the total volume of the group of bubbles (i.e., only the first arriving bubble contributes to the radar measurement of the rapid expansion). Due to the inertia of the large magma mass in the conduit underneath the lake, which would need to be displaced by tens of meters in the short time frame of an explosion, we consider the first hypothesis as unlikely.

[67] Supporting the latter hypothesis, laboratory experiments in liquid-filled tubes [*James et al.*, 2006] suggest that the disruption of a gas slug [*Ripepe et al.*, 1993; *Rowe et al.*, 2000] into multiple sub-bubbles will commonly occur when a rising slug encounters abrupt conduit widening, such as that which occurs where the Erebus magma conduit widens upon its final ascent to the lava lake [*Dibble et al.*, 2008]. While the observed widening of the conduit accounts for the minimal (i.e., a few meters) lake surface rise before explosions, the inferred bubble splitting effect can account for the double peak in the acceleration curve (Figure 9c), with subsidiary bubbles arriving and possibly partially merging prior to shell rupture.

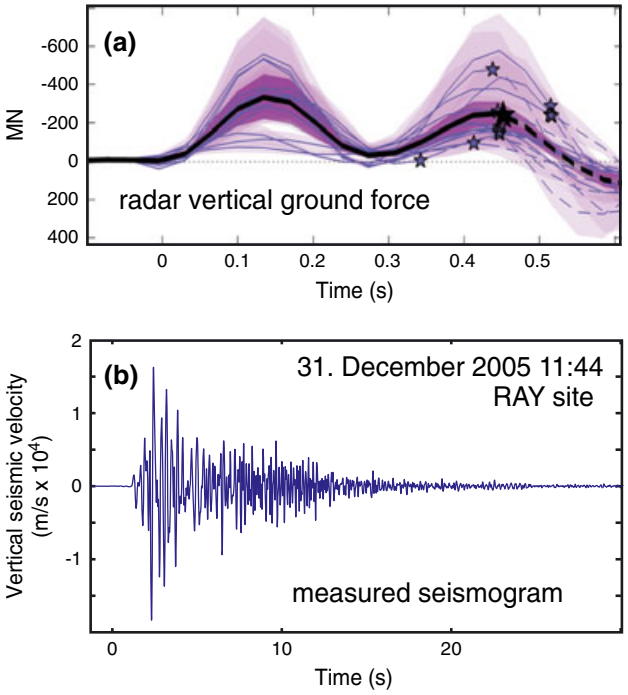

Figure 12. (a) Vertical ground reaction force generated by explosions from (13), where a negative force means "down." The black line shows the mean of all traces, its dark purple error shade indicates the median width of all error shades. Light purple shades show individual error ranges. (b) Vertical component velocity seismogram, recorded on the crater rim, showing a typical highly scattered and emergent waveform for a lava lake explosion.

[68] It is tempting to interpret the observed double acceleration peak as an oscillation (with period ∼0.3 s) of the heavy magma shell on the underlying gas acting as a spring [e.g., *Vergniolle and Brandeis*, 1994; *Lane and Gilbert*, 2008]. However, according to the oscillation model suggested by *Vergniolle et al.* [1996, equation (5)], the expected oscillation periods for the given approximate shell and gas masses at Erebus are in the order of several seconds, and thus cannot explain the ∼0.3 s double peak as a gas oscillation (for more details, see *Gerst* [2010], section 9.8.3).

[69] A further constraint that the above derived gas volumes impose on hypotheses for gas pocket formation at Erebus is that, when hypothesizing that the gas pocket could alternatively be formed by a shallow collapsing foam layer instead of a deeper-rooted slug, such a foam layer would have to be several tens of meters thick. Any model that supports such a hypothesis would have to include such a thick foam layer at shallow depths, which appears an unlikely scenario.

4.4. Seismic Signals and Energy

[70] Vertical ground reaction forces resulting from bubble explosions were calculated from (13), acting downward on the ground in the range of 100–800 MN (Figure 12a). These reaction forces, applied to the complex topography and elastic structure of the volcano, generate seismic surface and body waves that rapidly scatter (within a few seconds) within the volcano due to its high degree of internal heterogeneity [*Chaput et al.*, 2012]. The observed seismic wavefield can furthermore be expected to include secondary source contributions generated by ejecta falling back into the crater and conduit, magma film interaction with the conduit wall, seismoacoustic coupling with the infrasonic field, and seismic radiation arising from dilatational forces. However, such contributions to the wavefield are typically much smaller than those directly produced by a largely uncontained surface or near-surface explosion [e.g., *Kanamori et al.*, 1984].

[71] We next compare seismic observations with synthetic calculations predicted for the explosion reaction force, using our black-box approach described in section 2.4.7 and therefore avoiding detailed assumptions on the source coupling.

[72] As is typical for volcanic environments, short period seismograms from explosions at Erebus are characterized by an emergent wavefield with most energy between 1 and 10 Hz, and seismograms show a long-tailed (typically 20–30 s) coda of coupled surface and body waves (Figure 12b). These characteristics arise from strong seismic scattering from interspersed ash, bomb, and lava layers, its near-summit magmatic system, and its topography [e.g., *Rowe et al.*, 2000; *Aster et al.*, 2003; *La Rocca et al.*, 2001; *Chaput et al.*, 2012]. Such strongly developed coda signals on volcanoes and elsewhere are commonly found to be dominated by *S* waves with some coupled Rayleigh wave components [e.g., *Del Pezzo et al.*, 1997].

[73] Lava lake explosions at Erebus volcano ubiquitously produce very long period (VLP) signals that arise from at least two distinct mechanisms [*Aster et al.*, 2003]. The first VLP component is associated with the terminal bubble rise and expansion through the lava lake. This preeruptive signal is correspondingly short-lived (a few seconds) and variable in its polarity and amplitude, reflective of complex and countervailing conduit forces in the last few seconds prior to an eruption. The second and most significant VLP component is, in contrast, highly repeatable in its seismic signature and arises from reaction and pressurization forces applied internally to the volcano during post-eruptive refill of the lava lake system as it reestablishes gravitational equilibrium. Moment rate tensor inversion [*Aster et al.*, 2008] indicates a source zone for this refill-associated signal that is ∼400 m to the west-northwest and ∼400 m below the lava lake. This source zone is attributed to a geometric conduit feature [*Zandomeneghi et al.*, 2013] that concentrates forces arising during refill from a deeper magma reservoir.

[74] Although they are very prominent in displacement seismograms, VLP signals are a second-order feature of velocity seismograms because of their low frequency content [*Aster et al.*, 2003; *Rowe et al.*, 1998]. Thus, seismic energy, which is proportional to velocity squared (19), overwhelmingly resides in the spectrally distinct (∼1–10 Hz) shorter period components of the seismic wavefield that are generated by bubble expansion forces, and which we model for energy balance purposes below.

[75] The detailed elastodynamic and fluid dynamic coupling between eruptive forces and the underlying conduit system, as well as the irregular crater floor that gives rise to seismic radiation, presents a challenging modeling problem [*Nishimura and Chouet*, 2003]. In addition, the details of coupling between elastic waves within the conduit magma

and the substantially unknown internal geometry of the volcano make deterministic modeling of the seismic wavefield unfeasible.

[76] We can, however, perform an order of magnitude predictive comparison between theory and observation in the 1–10 Hz frequency rage by applying a shallow vertical force (depth z = 50 m) using the average time function shown in Figure 12a. In addition to the body wave source model of *Haskell* [1964] described in (14), we considered the seismic effects of applying this force to the surface of an elastic half-space (Lamb's problem) to calculate the seismic response using reasonable bulk properties for the summit region of the volcano at the position of the lava lake [*Johnson*, 1974; *Dibble et al.*, 1994, seismic velocities v_p = 2.2 km/s; v_s = 1.27 km/s; density ρ = 2400 kg/m^3].

[77] A Lamb's problem vertical force applied to a uniform half space primarily generates short period Rayleigh waves with an r^{-1} decay with distance. However, as described above, scattering rapidly equilibrates the observed wavefield into an extended coda that predominantly consists of body waves. Observed seismic energy decays with distance as approximately r^{-2}, consistent with body wave energy dispersal through an approximately half-spherical space, rather than the r^{-1} spreading expected for surface waves. We suggest that Rayleigh waves are not highly excited by these explosions due to the topography and heterogeneity of the volcano, and that a Lamb's problem formulation is therefore inappropriate for modeling this system. We thus use the body wave half-space corrected formulation (14) for comparison with observed seismic energies.

[78] To estimate radiated seismic energy from recorded seismograms, we assumed predominantly shear waves and used seismograms from the displayed 31 December 2005 explosion (Figure 12b). We applied the formula of *Kanamori et al.* [1993], which assumes shear-wave radiation into a half space:

$$E_{\text{seis}} = 2\pi r^2 \rho v_s \int \dot{u}^2(t)\,\mathrm{d}t. \tag{19}$$

Here $\dot{u}$ is the seismic velocity observed at a station located at a range of r from the explosion, v_s is the shear wave velocity, ρ is the rock density, and the integral is calculated for the entire seismogram. This yielded seismic station estimates ranging from 47 to 179 kJ, with a station average of 96 kJ. This value is in reasonable agreement with seismic energies of ∼50 kJ to 100 kJ inferred from radar measurements and calculations shown in (Figure 11a) obtained using (14).

4.5. Infrasonic Signals

[79] Erebus infrasonic waveforms are readily recorded at ranges up to several kilometers (Figure 13), and despite a notable variability in the signals with respect to time and receiver location (as previously noted by, e.g., *Rowe et al.* [2000]; *Johnson et al.* [2008], and possibly influenced by directivity effects, *Gerst et al.* [2008]), they show a relatively simple signature reflective of a largely compact source (< 1 Hz; e.g., *Vergniolle and Brandeis* [1994]; *Hagerty et al.* [2000]; *Johnson* [2003]; *Johnson et al.* [2008]). Due to the crater geometry and other site considerations, individual microphones were deployed at varying distances from the lava lake (for a detailed description of the microphone locations, see *Jones et al.* [2008], and section A1 for specifications).

[80] To better facilitate the comparison of observed and predicted acoustic signals, we have shifted all recorded acoustic signals by a fixed amount of time to represent a recording on the crater rim at 300 m distance from the lake center. This time shift was not adjusted for individual explosions, but was determined only once per station and remained fixed for the entire data set (signal travel times from lake to receiver were found to be 0.93 s, 0.99 s, 1.74 s, and 2.43 s for RAY, SHK, E1S1, and E1S2 sites, respectively). Similarly, we have scaled the recorded amplitudes to that same distance, using a simple r^{-1} correction, where r is the distance from the lava lake.

4.5.1. Preburst Infrasound

[81] As discussed at the beginning of this section, models that explain the generation of the infrasonic signal of a bubble burst-driven (e.g., Strombolian) explosion through a mechanism involving multiple oscillations of the intact bubble surface around an equilibrium radius [e.g., *Vergniolle and Brandeis*, 1994; *Vergniolle et al.*, 1996] can be ruled out for Erebus, and thus appear unlikely for volcanoes with a similar underlying source mechanism.

[82] The model detailed in this study allows for calculation of the expected infrasonic wavefield for each explosion, shown superimposed on the observed infrasound traces in Figure 13. Red lines show the expected infrasound signals of all type I explosions, as they would be observed in a half-space (using (17) and (18)) at a line-of-sight distance of 300 m and an elevation angle of 39° (to reflect the location of a microphone on the crater rim). At these close ranges, we assume negligible atmospheric path effects [*Johnson et al.*, 2008]. We note that crater wall echoes likely affect the signals at times > 1 s after onset [*Johnson et al.*, 2008], which is not considered in our simple half-space model. Also, the effect of atmospheric absorption [*Pierce*, 1981] on the pressure amplitude was neglected, which is validated and common practice for infrasound propagating over short distances [e.g., *Vergniolle et al.*, 1996; *Johnson et al.*, 2008].

[83] The model predicts significant infrasonic radiation prior to shell burst (shown as stars in Figure 13) due to the rapid preburst bulging of the lava lake surface. Radar data are only valid for describing the bulging of the magma shell before its rupture, thus, the traces end at burst time. Before burst, infrasound resulting from the bulging creates pressure disturbances with amplitudes of several tens of Pascals at the range of the crater rim.

[84] At the time of shell burst, a number of short-lived gas jets emerge from the fragmenting shell that will most likely generate a complex near-field structure at high frequencies, but they are not expected to have a significant influence on our measurements on the crater rim at the frequencies of interest.

[85] The predicted and measured acoustic pressure signals shown in Figure 13 match well for most type I explosions up until burst time. The recorded signal is typically close to that of a monopole source, which is in accordance to earlier findings at Erebus [*Johnson et al.*, 2008] that attribute the initial ∼0.5 s pulse of the infrasound signal to a monopole volume source.

[86] When examining the fit in detail, it is notable that the typical double peak pattern in the predicted acoustic pressure signal (resulting from the double acceleration peak that is typical for type I explosions) often correlates

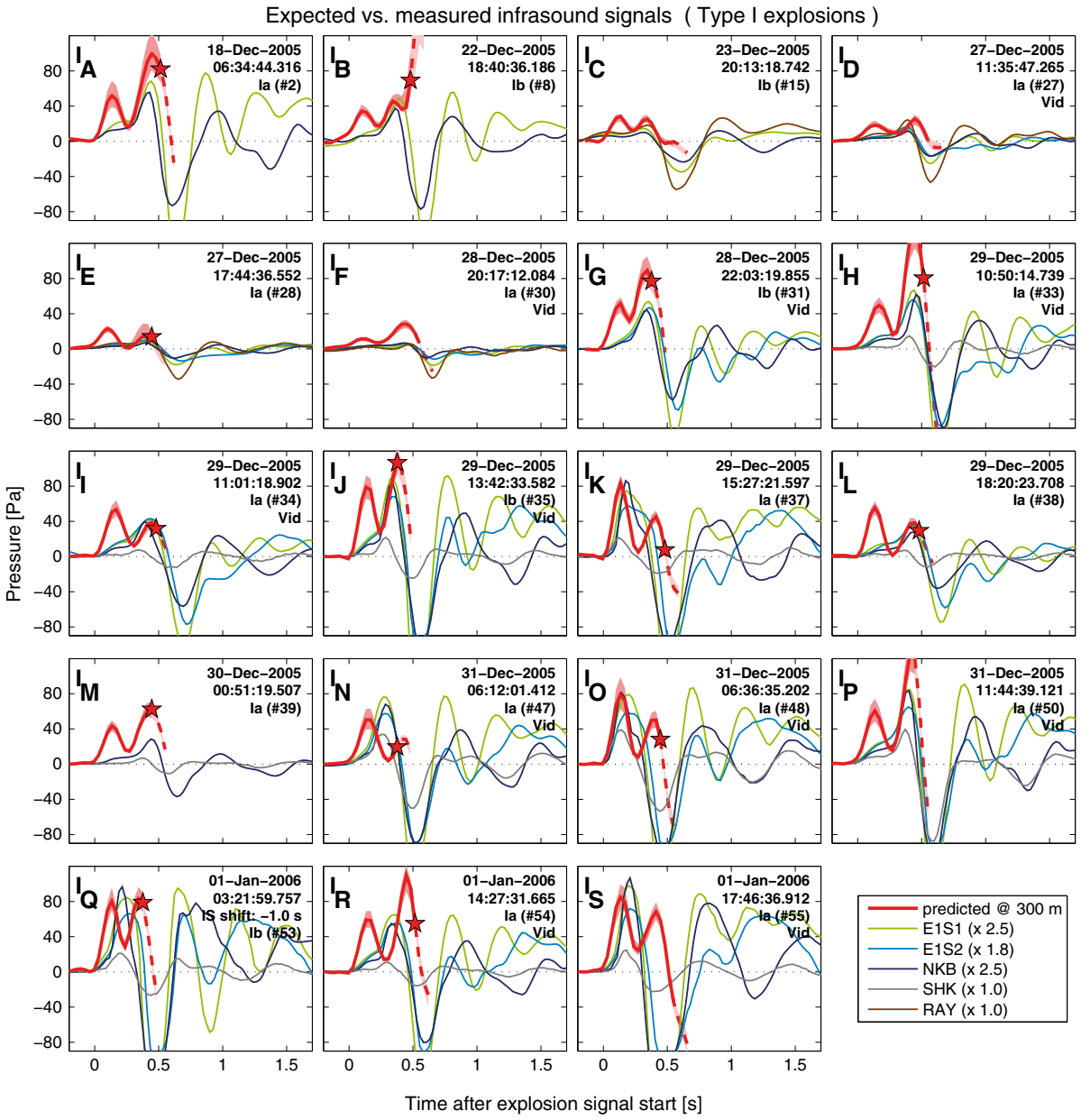

Figure 13. *Expected versus measured infrasound signals (type I).* Thick red lines show the acoustic pressure signal predicted by the model, calculated from radar data (error range shown as red shade). Thin lines show recorded unfiltered broadband infrasound signals from different microphone sites. Traces were corrected in travel time and amplitude to a common virtual distance of 300 m assuming ambient sound speed and r^{-1} geometric spreading (note that neither onset time nor amplitude was fitted to the data but arose directly from the modeling).

with a distinctive plateau, or change in curvature, in the observed infrasound from type I explosions [similar to waveforms observed by *Rowe et al.*, 2000; *Johnson et al.*, 2008]. Given the simplicity of the model and the absence of arbitrarily fitted parameters, this matches not only in absolute amplitude but also in waveform is noteworthy (e.g., Figure 13 I_A).

4.5.2. Post-Burst Infrasound

[87] As a second main feature of the infrasonic signal, we suggest that its post-slug-burst waveform can be used to estimate properties of the bursting gas slug. Experiments show that a $\lambda/4$ resonator is formed when a membrane above a pressurized gas filled cylindrical cavity suddenly bursts [*Vidal et al.*, 2006]. We propose that this is a likely modulator of sound following the burst of the magma shell above a pressurized gas slug at Erebus.

[88] From total slug volumes calculated above, slug lengths (and therefore cavity lengths) of up to 100 m are expected. Assuming that the cavity contains a 60/40 molar mixture of water vapor and CO_2 at a temperature of 800°C, the intracavity speed of sound will be $\sim$ 600 m/s. For a 100 m-deep cavity, this leads to a fundamental resonance frequency of $\sim$1.5 Hz. Employing equation (4) of *Vidal et al.* [2006], using a kinematic viscosity of 2×10^{-4} m^2/s and

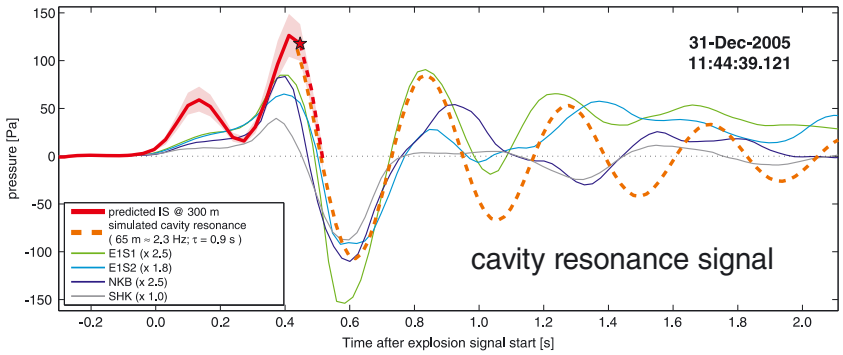

Figure 14. Cavity resonance signal modeling. As in Figure 13, thin lines show recorded unfiltered pressure for a typical Erebus explosion (Figure 13 I_P). Accordingly, the thick red line shows the infrasonic pressure signal predicted from modeling of radar data arising from expansion of the intact magma shell (part 1 of the dual mechanism). Additionally, the orange dashed line shows the subsequent predicted infrasonic pressure signal for a 65 m deep, 40 m wide resonating cavity, accounting for the infrasound signal after the shell burst (part 2 of the dual mechanism). Note that (unmodeled) crater wall echoes are expected to influence the signal after about 1 s.

a Prandtl number of 0.8 (appropriate for hot water vapor), we calculate, as an example, a characteristic damping time (for the main mode) of 3.4 s for a 100 m deep cavity, and 0.4 s for a 50 m deep cavity (for both assuming a 40 m wide mouth inferred from the lava lake diameter, see Figure 2).

[89] Figure 14 shows good agreement between the expected signal of a 65 m deep resonating cavity for an initial pressure amplitude of 80 Pa at the crater rim, superimposed on the real infrasound signal, along with the above discussed predicted pre-burst signal. The synthetic resonator signals match the observed signals both in frequency and damping behavior.

[90] Laboratory experiments [*Vidal et al.*, 2006, 2010] show that for slowly bursting (i.e., high inertia) membranes, the resonance amplitude is typically only a small fraction of the outward propagated initial cavity pressure and is highly sensitive to local conditions and thus difficult to predict. This is further complicated by the influence of the burst time of a bubble, and therefore of the remaining pressure in the cavity on the amplitude of the post-burst infrasonic signal (i.e., a cavity which, due to a late burst, is close to pressure equilibrium with the atmosphere will not oscillate with high amplitudes). This effect can explain the observation of variable waveforms, and therefore also explains the often highly variable correlation between seismic and infrasonic amplitudes during volcanic explosions [*Rowe et al.*, 2000; *Johnson et al.*, 2005; *Scharff et al.*, 2008] in addition to possible directivity effects [*Gerst et al.*, 2008]. Also, an important consequence of this is that, while the signal's frequency content offers a method to measure slug length and conduit width, the estimation of preburst slug pressure and gas energy from distant pressure recordings is greatly complicated by the variability of amplitudes. We therefore highlight the importance of the frequency content of an infrasound signal over its amplitude.

4.5.3. Summary of Combined Infrasonic model

[91] In summary, we suggest that infrasonic signals of large bubble burst explosions at Erebus (and possibly for discrete eruptions at Strombolian volcanoes in general) are best explained by a dual mechanism, consisting of a preburst volumetric source signal generated by the expanding magma shell, as well as a post-burst signal component that is spectrally shaped by a resonating cavity. Furthermore, by providing the resonance frequency of post-burst infrasound emissions, our model provides a relatively simple tool to estimate slug length from a remotely measured infrasonic spectrum, and by estimating the conduit width from the signal decay time, a useful estimate of the gas volume of single explosions can be calculated.

5. Discussion and Conclusions

[92] We show that a multiparameter data set incorporating Doppler radar, seismic, infrasonic, and video observations can be effectively integrated to provide novel and fundamental information about the phenomenology and energy balance in volcanic eruptions. This includes monitoring in situ explosion parameters during this critical first second of impulsive eruptions in near real-time while facilitating consistency checks between eruptive process modeling (e.g., calculated forces compared to radiated seismic and acoustic energies) for various component observations.

[93] For these large bubble burst explosions, ejecta energy comes from large pressurized gas slugs rising to the conduit surface before exploding. At Erebus, we find that these slugs explode at moderate overpressure of a few atmospheres, release several metric tons of gas, and have typical total energy releases of up to 10^{12} J (equivalent to the energy released by ~1 kiloton of TNT). Advected thermal energy, together with the kinetic and potential energy of the ejecta, dominates the energy budget.

[94] Preburst bubble pressures at volcanoes with different magma compositions will generally be dependent on their respective magma viscosities and conduit diameters [*Lane and Gilbert*, 2008], which can be estimated [*Del Bello et al.*, 2012]. Thus, we expect that preburst gas pressures can similarly be determined for those volcanoes. Detailed energy partitioning during explosions depends on multiple factors that will naturally vary from volcano to volcano. However, we suggest that the order of magnitude breakdown in the energy budget should be a robust feature of eruptive events that are driven by this large bubble burst mechanism.

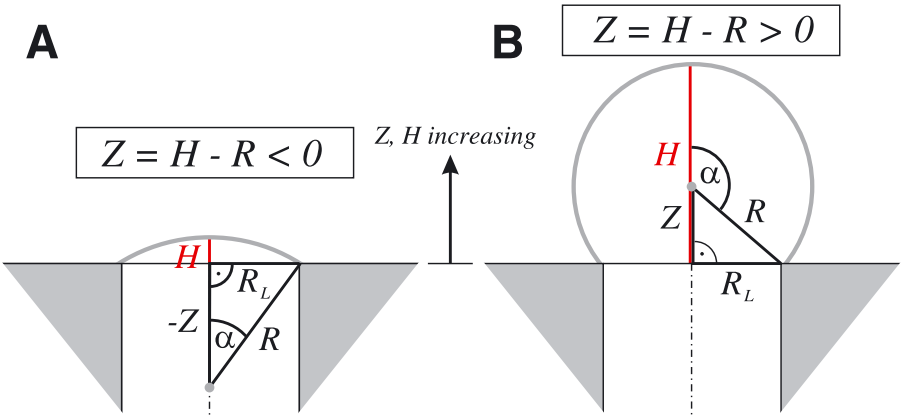

Figure A1. Model geometry of the spherically expanding gas bubble.

[95] Doppler radar, together with a simple eruption model, explains the infrasound signal generated during the first moments of an eruption as a result of a dual mechanism. We find that, following the initial infrasound signal generation by an expanding bubble shell, it can be explained by a $\lambda/4$ resonating gas slug cavity within the evacuated conduit. This suggests a method for determining slug lengths and erupted gas volumes from distant infrasound observations.

[96] Modeled vertical ground forces are consistent with observed amplitudes of seismic signals associated with explosions.

[97] The above findings show that high-speed Doppler radars have the potential to play a major role in future real-time volcano monitoring as well as in detailed studies of volcanic systems.

Appendix A: Model and Experimental Details

A1. Infrasound Microphone Specifications

[98] The low-frequency microphones utilize amplified, temperature-compensated Honeywell MEMS transducers (model DC001NDR5) operated in a differential mode with one pressure port vented to the atmosphere through 50 micron capillary tubing. Linear dynamic range is at least +/−250 Pa and frequency response is flat within the band of interest up to Nyquist (< 0.25 Hz to 20 Hz). No digital filter was applied to the signals shown in this manuscript.

A2. Derivation of the Shell Expansion Rate

[99] The position Z of the geometrical center of the spherical shell section lies beneath the undisturbed lake level surface during the early stages of an explosion, but will eventually move up and cross this plane at some stage. This leads to two geometrically different situations that need to be distinguished (Figures A1a and A1b), so care must be taken not to introduce inconsistencies when moving from geometry A ($Z < 0$) to geometry B ($Z > 0$). The following parameter relations are valid for all Z:

$$Z = H - R \tag{A1}$$

$$R = \frac{H}{2} + \frac{R_L^2}{2H} \tag{A2}$$

$$\alpha = \arccos\left(\frac{R-H}{R}\right) \tag{A3}$$

$$H = \begin{cases} R + \sqrt{R^2 - R_L^2} & : \quad Z \geq 0 \\ R - \sqrt{R^2 - R_L^2} & : \quad Z < 0 \end{cases}, \tag{A4}$$

where R is the shell radius and α is the opening angle of the shell cap (Figure A1). It is always equal to or larger than the lake radius ($R \geq R_L$; $H \geq 0$).

[100] The volume V_{cap} surrounded by the shell and the outside surface area A_{cap} of the spherical cap are

$$V_{\text{cap}} = H^2\pi\left(R - \frac{H}{3}\right) = \frac{\pi}{6}H^3 + \frac{\pi R_L^2}{2}H \tag{A5}$$

$$A_{\text{cap}} = 2\pi R^2(1-\cos\alpha) = 2\pi RH = \pi\left(H^2 + R_L^2\right). \tag{A6}$$

V_{cap}, which increases during an explosion, should not be confused with V_m (Figure 2), which is the *constant* volume of the magma in the cap shell, i.e.,

$$V_m = \frac{m_m}{\rho_m} \approx h\,A_{\text{cap}}, \tag{A7}$$

where m_m is the total mass of the magma in the shell, and ρ_m is its density. The magma volume can be approximated by the product of the shell thickness h and its surface area A_{cap}, because the shell thickness is always much smaller than the bubble radius ($h \ll R_L \leq R$).

[101] As the bubble geometry is changing in time, the above parameters (H, R, V_{cap}, and h) are functions of time; therefore, their time derivatives can be calculated:

$$\dot{R} = \dot{H}\left(\frac{1}{2} - \frac{R_L^2}{2H^2}\right) \tag{A8}$$

$$\dot{H} = \dot{R}\left(1 + \frac{R(t)}{H-R}\right) \tag{A9}$$

$$\dot{V}_{\text{cap}} = \frac{\pi}{2}\dot{H}(H^2 + R_L^2). \tag{A10}$$

[102] The Zenith height $H(t)$ and its time derivatives $\dot{H}(t)$, and $\ddot{H}(t)$ shall be the main parameters describing the bubble geometry and its movement; therefore, R and Z will be eliminated from all final equations.

[103] Some of the following equations (e.g., for calculating the total kinetic energy of the cap) will require to integrate over the whole volume of the magma shell (i.e., the constant volume of magma V_m in the shell, *not* the total (gas) volume surrounded by the cap V_{cap}). In order to facilitate these integrals by making use of the special symmetry of the

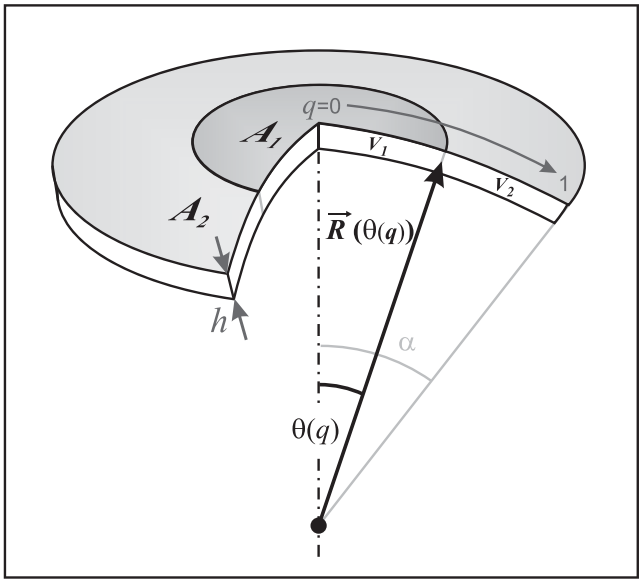

Figure A2. Model parametrization geometry. The surface length parameter q was chosen such that it increases linearly with the enclosed shell volume V_1, thus facilitating a simpler analytic solution for most energy terms.

geometrical shape, we will introduce the auxiliary parameter $q \in [0 \ldots 1]$, where $q = 0$ defines the zenith of the cap, and $q = 1$ defines the edge of the cap (Figure A2). As a requirement, q shall be a linear measure of the volume of magma enclosed in the shell (i.e., V_1 in Figure A2) along the cap surface, starting from the zenith point (enclosing a volume of zero) and increasing toward the edge (enclosing the full cap volume). Therefore, the following assumption must be fulfilled:

$$q = \frac{V_1}{V_m} = \frac{V_1}{V_1 + V_2} = \frac{A_1}{A_1 + A_2}, \tag{A11}$$

where V_1 is the cap volume enclosed by a circle defined by q, V_2 is the remaining volume, and $V_m = V_1 + V_2$ is the total volume of the magma shell (A7). A_1 and A_2 are the upper surface areas of shell sections V_1 and V_2. Since the thickness $h(t)$ is small compared to the lake radius R_L, the volumes can be approximated as $V_{1,2} \approx h\, A_{1,2}$ (see A7). The surface areas are given by

$$A_1(q) = \int_{A_1} \mathrm{d}A = \int_0^{2\pi} \int_0^{\theta(q)} R^2 \sin\theta' \, \mathrm{d}\theta' \mathrm{d}\Phi = 2\pi R^2 (1 - \cos\theta(q)) \tag{A12}$$

$$A_{\mathrm{cap}} = A_1 + A_2 = 2\pi R^2 (1 - \cos\alpha), \tag{A13}$$

where θ is the angle between $\vec{R}$ and the vertical. Therefore, with (A3) and (A11) we find

$$q(\theta) = \frac{1 - \cos\theta}{1 - \cos\alpha} = \frac{R}{H}(1 - \cos\theta) \tag{A14}$$

or

$$\theta(q) = \arccos\left(1 - \frac{qH}{R}\right). \tag{A15}$$

[104] The volume form $\mathrm{d}V$ for integrals over a shell with thickness $h \ll R$ can be transferred if the function to be integrated is not a function of azimuth Φ. Thus, using (A11) (where $V(q) = V_1 = qV_m$), $\mathrm{d}V$ can be replaced by

$$\mathrm{d}V = V_m \, \mathrm{d}q. \tag{A16}$$

[105] With the parameter q, any given point in the (x, z)-plane can now be defined in the form $\vec{r} = \vec{r}(q)$, where $q \in [0 \ldots 1]$ (Figure A2). Due to the symmetry around the vertical axis we can use two-component vectors of the form $\vec{r} = \binom{r_x}{r_z}$, each representative for a ring of points on the shell. As shown in Figure A3, $\vec{r}(q)$ can be written as

$$\vec{r}(q) = \begin{pmatrix} r_x \\ r_z \end{pmatrix} = \vec{Z} + \vec{R}(\theta(q)) \tag{A17}$$

$$= \begin{pmatrix} 0 \\ Z \end{pmatrix} + \begin{pmatrix} R\sin\theta(q) \\ R\cos\theta(q) \end{pmatrix}, \tag{A18}$$

and using (A15) and (A1) eventually leads to (3) and (4) above. Due to (A16), q will be eliminated when integrating over the shell surface volume, which is necessary when subsequently deriving the shell's energy terms.

A3. Radar Cutoff Velocity

[106] We will now determine the radar cutoff velocity from model parameters. First, it is necessary to calculate the velocity component of a given surface point $\vec{r}(q)$ as seen from the radar. We define a unit vector

$$\hat{\vec{r}}_R = \begin{pmatrix} \hat{r}_{R,x} \\ \hat{r}_{R,z} \end{pmatrix} = \begin{pmatrix} \cos\phi_R \\ \sin\phi_R \end{pmatrix} \tag{A19}$$

pointing from the source, i.e., from the magma cap toward the radar, which is also located in the (x, z)-plane. Because the beam spread is only $\sim \pm 1.5°$ and the distance to the radar device ($\sim$300 m) is significantly larger than the target region, we consider this unit vector to be constant within the target region. ϕ_R is the elevation angle (inclination) of the radar as seen from the source (Figure A3). The speed of surface point $\vec{r}$ as measured by the radar is simply the projection of $\dot{\vec{r}}$ onto the unit vector pointing in radar direction:

$$v_R(q) = \dot{\vec{r}}(q) \cdot \hat{\vec{r}}_R = \begin{pmatrix} \dot{r}_x(q) \\ \dot{r}_z(q) \end{pmatrix} \cdot \begin{pmatrix} \cos\phi_R \\ \sin\phi_R \end{pmatrix} \tag{A20}$$

$$= \dot{H} \underbrace{\left(\frac{qH(1-q)\cos\phi_R}{\sqrt{qH^2(1-q) + qR_L^2}} + (1-q)\sin\phi_R \right)}_{Q} \tag{A21}$$

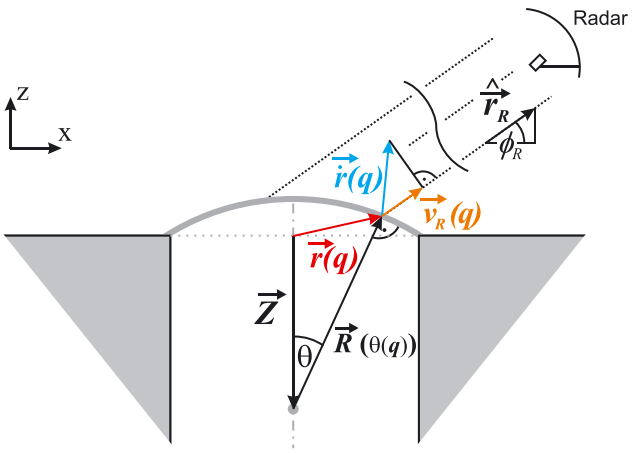

Figure A3. Radar view angle geometry.

As argued above, the cutoff velocity in the radar spectrum $v_{\mathrm{R,cut}}$ is the maximum of $v_R(q)$ with respect to q:

$$v_{\mathrm{R,cut}} = \dot{H} \max_{q \in q_0, q_1} \Big(Q(q, H) \Big), \tag{A22}$$

where $[q_0 \ldots q_1]$ defines the area of the cap that is observed by the radar beam. If the radar beam covers the whole area between zenith and cap edge, then q is allowed to vary over its whole range $[0 \ldots 1]$ (Figure A2). By reversing this equation, the zenith velocity $\dot{H}(t)$ at time t can be determined from $v_{\mathrm{R,cut}}(t)$, leading to (5). This equation establishes a way to iteratively calculate the cap zenith height H and velocity $\dot{H}$ directly from radar observations ($v_{\mathrm{R,cut}}$), starting from the initial condition of $H = 0$ for every explosion.

Notation

A_{cap} Surface area of bubble cap shell.
c_a Speed of sound in atmosphere.
$c_{p,m}$ Specific heat capacity at constant pressure (magma).
E, W Energy (general).
E_{atm} Sonic energy radiated into atmosphere.
E_{diss} Energy dissipated in magma shell.
E_{surf} Surface energy of magma shell.
E_{kin} Kinetic energy of magma shell.
E_{pot} Potential energy of magma shell in Earth's gravity.
E_{seis} Seismic energy radiated into ground.
E_{therm} Thermal energy of magma shell.
E_{total} Total dynamic energy released during an explosion.
$F_{\mathrm{ground,z}}$ Vertical ground force.
H Zenith height of magma cap.
h Current thickness of bubble shell.
h_0 Initial thickness of bubble shell.
m_m Total mass of the magma in bubble shell.
$\hat{\vec{n}}$ Surface normal unit vector.
$P, \dot{E}$ Power (general, J/s).
p_{gas} Overpressure inside a gas bubble.
q Model parameter of magma cap.
$R, \vec{R}$ Radius/radial vector of a spherical bubble.
$\vec{r}$ Position vector (general).
$\dot{\vec{r}}$ Velocity (general).
$\ddot{r}, \dot{v}$ Acceleration (general).
R_L Lava lake radius.
$\vec{v}$ Velocity (general).
t Time (general).
V_{cap} Volume of gas in bubble cap.
V_{gas} Volume of a gas bubble (consisting of V_{cap} and slug tail volume).
V_m Volume of magma in shell.
v_R Velocity component along radar beam.
$v_{\mathrm{R,cut}}$ Radar cutoff velocity.
W_{gas} Pressure-volume work (magmatic gas).
Z Vertical coordinate of magma cap center.
v_p seismic P wave velocity.
v_s seismic S wave velocity.
μ_m Viscosity of magma.
Φ Azimuth (general).
ϕ_R Elevation angle between radar beam and the horizontal.
ρ Density (general).
ρ_a Density (atmosphere).
ρ_m Density (magma).
σ Standard error interval (general).

[107] **Acknowledgments.** We thank UNAVCO, the IRIS PASSCAL Instrument Center at New Mexico Tech for support at Erebus volcano, and the METEK Company for supporting our radar measurements. Donations of equipment from Extreme CCTV, VideoComm Technologies and Amphenol Air LB helped our hardware development. We thank M. Vöge and L. Scharff for essential input from the first moments of this project, as well as Raytheon Polar Services Company individuals and groups at McMurdo together with many more helpers from Hamburg University and NMT who made this field effort possible. This research was supported by NSF Grants OPP-0116577, OPP-0229305, ANT-0538414, ANT-0838817, and ANT-1142083, by New Mexico Tech Research and Economic Development, and by the German Science Foundation through project Ho1411-16 1-3. J.J. was supported by NSF CAREER grant 1151662. The facilities of the IRIS Consortium are supported by the National Science Foundation under Cooperative Agreement EAR-0552316 and by the Department of Energy National Nuclear Security Administration. A particular thanks goes to S. Lane, Andre Revil, and an anonymous reviewer for their constructive comments.

References

Aster, R., S. Mah, P. Kyle, W. McIntosh, N. Dunbar, J. Johnson, M. Ruiz, and S. McNamara (2003), Very long period oscillations of Mount Erebus Volcano, *J. Geophys. Res.*, *108*(B11), 2522, doi:10.1029/2002JB002101.

Aster, R., et al. (2004a), New instrumentation delivers multidisciplinary real-time data from Mount Erebus, Antarctica, *Eos Trans. AGU*, *85*(10), 97–101, doi:10.1029/2004EO100001.

Aster, R., D. Zandomeneghi, S. Mah, S. McNamara, D. Henderson, H. Knox, and K. Jones (2008), Moment tensor inversion of very long period seismic signals from Strombolian eruptions of Erebus Volcano, *J. Volcanol. Geotherm. Res.*, *177*(3), 635–647, doi:10.1016/j.jvolgeores.2008.08.013.

Blackburn, E., L. Wilson, and R. Sparks (1976), Mechanism and dynamics of Strombolian activity, *J. Geol. Soc. London*, *132*, 429–440, doi:10.1144/gsjgs.132.4.0429.

Calkins, J., C. Oppenheimer, and P. Kyle (2008), Ground-based thermal imaging of lava lakes at Erebus Volcano, Antarctica, *J. Volcanol. Geotherm. Res.*, *177*(3), 695–704, doi:10.1016/j.jvolgeores.2008.02.002.

Chaput, J., H. Zandomeneghi, H. Knox, R. Aster, and P. Kyle (2012), Imaging of Erebus Volcano using body wave seismic interferometry of Strombolian eruption coda, *Geophys. Res. Lett.*, *39*, L07304, doi:10.1029/2012GL050956.

Chouet, B., G. Saccorotti, M. Martini, P. Dawson, G. De Luca, G. Milana, and R. Scarpa (1997), Source and path effects in the wave fields of tremor and explosions at Stromboli Volcano, Italy, *J. Geophys. Res.*, *102*(B7), 15,129–15,150

Csatho, B., T. Schenk, W. Krabill, T. Wilson, G. McKenzie, C. Hallam, S. Manizade, and T. Paulsen (2005), Airborne laser scanning for high-resolution mapping of Antarctica, *Eos Trans. AGU*, *86*(25), 237–238.

Del Bello, E., E. Llewellin, J. Taddeucci, P. Scarlato, and S. Lane (2012), An analytical model for gas overpressure in slug-driven explosions: Insights into Strombolian volcanic eruptions, *J. Geophys. Res.*, *117*, B02206, doi:10.1029/2011JB008747.

Del Pezzo, E., M. La Rocca, and J. Ibanez (1997), Observations of high-frequency scattered waves using dense arrays at Teide Volcano, *Bull. Seismol. Soc. Am.*, *87*(6), 1637–1647.

Dibble, R. (1994), Velocity modeling in the erupting magma column of Mount Erebus, Antarctica, in *Volcanological and Environmental Studies of Mount Erebus, Antarctica, Antarct. Res. Ser.,* vol. 66, edited by P. Kyle, pp.17–33, AGU, Washington, D.C.

Dibble, R., B. O'Brien, and C. Rowe (1994), The velocity structure of Mount Erebus, Antarctica, and its lava lake, in *Volcanological and Environmental Studies of Mount Erebus, Antarctica, Antarct. Res. Ser.,* vol. 66, edited by P. Kyle, pp. 1–16, AGU, Washington, D.C.

Dibble, R., P. Kyle, and C. Rowe (2008), Video and seismic observations of Strombolian eruptions at Erebus volcano, Antarctica, *J. Volcanol. Geotherm. Res.*, *177*(3), 619–634, doi:10.1016/j.jvolgeores.2008.07.020.

Dingwell, D., N. Bagdassarov, G. Bussod, and S. Webb (1993), Magma rheology, in *Experiments at High Pressure and Applications to the Earth's Mantle,* vol. 21, edited by R. Luth, pp. 131–196, Mineral. Assoc., Canada.

Divoux, T., V. Vidal, F. Melo, and J. Géminard (2008), Acoustic emission associated with the bursting of a gas bubble at the free surface of a non-Newtonian fluid, *Phys. Rev.*, *77*, 056310.

Ehrenfried, K. (2003), *Skript zur Vorlesung*, Strömungsakustik I, Tech. Univ., Berlin.

Garcés, M., and S. McNutt (1997), Theory of the airborne sound field generated in a resonant magma conduit, *J. Volcanol. Geotherm. Res.*, *78*(3-4), 155–178, doi:10.1016/S0377-0273(97)00018-8.

Garcés, M., A. Harris, C. Hetzer, J. Johnson, S. Rowland, E. Marchetti, and P. Okubo (2003), Infrasonic tremor observed at Kilauea Volcano, Hawai'i, *Geophys. Res. Lett.*, *30*(20), 2023, doi:10.1029/2003GL018038.

Gerst, A. (2010), The first second of a Strombolian volcanic eruption, PhD Thesis, Inst. für Geophys., Univ. Hamburg, Available at http://nbn-resolving.de/urn:nbn:de:gbv:18-42516.

Gerst, A., M. Hort, P. Kyle, and M. Vöge (2008), 4D velocity of Strombolian eruptions and man-made explosions derived from multiple Doppler radar instruments, *J. Volcanol. Geotherm. Res.*, *177*, 648–660, doi:10.1016/j.jvolgeores.2008.05.022.

Gurioli, L., A. J. L. Harris, B. F. Houghton, M. Polacci, and M. Ripepe (2008), Textural and geophysical characterization of explosive basaltic activity at Villarrica volcano, *J. Geophys. Res.*, *113*, B08206, doi:10.1029/2007JB005328.

Hagerty, M., S. Schwartz, M. Garcés, and M. Protti (2000), Analysis of seismic and acoustic observations at Arenal volcano, Costa Rica, 1995–1997, *J. Volcanol. Geotherm. Res.*, *101*, 27–65, doi:10.1016/S0377-0273(00)00162-1.

Harris, A., and M. Ripepe (2007), Synergy of multiple geophysical approaches to unravel explosive eruption conduit and source dynamics—A case study from Stromboli, *Chem. Erde Geochem.*, *67*(1), 1–35, doi:10.1016/j.chemer.2007.01.003.

Haskell, N. A. (1964), Total energy and energy spectral density of elastic wave radiation from propagating faults, *Bull. Seismol. Soc. Am.*, *54*(6), 1811–1841.

Hort, M., and R. Seyfried (1998), Volcanic eruption velocities measured with a micro radar, *Geophys. Res. Lett.*, *25*(1), 113–116, doi:10.1029/97GL03482.

Jaeger, J. (1964), Thermal effects of intrusions, *Rev. Geophys.*, *2*(3), 443–466.

James, M., S. Lane, B. Chouet, and J. Gilbert (2004), Pressure changes associated with the ascent and bursting of gas slugs in liquid-filled vertical and inclined conduits, *J. Volcanol. Geotherm. Res.*, *129*(1-3), 61–82, doi:10.1016/S0377-0273(03)00232-4.

James, M., S. Lane, and B. Chouet (2006), Gas slug ascent through changes in conduit diameter: Laboratory insights into a volcano-seismic source process in low-viscosity magmas, *J. Geophys. Res.*, *111*, B05201, doi:10.1029/2005JB003718.

Johnson, J., and J. Lees (2000), Plugs and chugs: Seismic and acoustic observations of degassing explosions at Karymsky, Russia and Sangay, Ecuador, *J. Volcanol. Geotherm. Res.*, *101*, 67–82.

Johnson, J., and M. Ripepe (2011), Volcano infrasound: A review, *J. Volcanol. Geotherm. Res.*, *206*, 61–69, doi:10.1016/j.jvolgeores.2011.06.006.

Johnson, J., M. Ruiz, J. Lees, and P. Ramon (2005), Poor scaling between elastic energy release and eruption intensity at Tungurahua Volcano, Ecuador, *Geophys. Res. Lett.*, *32*, L15304, doi:10.1029/2005GL022847.

Johnson, J., R. Aster, K. Jones, P. Kyle, and W. McIntosh (2008), Acoustic source characterization of impulsive Strombolian eruptions from the Mount Erebus lava lake, *J. Volcanol. Geotherm. Res.*, *177*(3), 673–686, doi:10.1016/j.jvolgeores.2008.06.028.

Johnson, J. B. (2003), Generation and propagation of infrasonic airwaves from volcanic explosions, *J. Volcanol. Geotherm. Res.*, *121*, 1–14, doi:10.1016/s0377-0273(02)00408-0.

Johnson, J. B., R. C. Aster, and P. R. Kyle (2004), Volcanic eruptions observed with infrasound, *Geophys. Res. Lett.*, *31*, L14604, doi:10.1029/2004GL020020.

Johnson, L. R. (1974), Green's function for Lamb's problem, *Geophys. J. R. Astron. Soc.*, *37*, 99–131.

Jones, K., J. Johnson, R. Aster, P. Kyle, and W. McIntosh (2008), Infrasonic tracking of large bubble bursts and ash venting at Erebus Volcano, Antarctica, *J. Volcanol. Geotherm. Res.*, *177*(3), 661–672, doi:10.1016/j.jvolgeores.2008.02.001.

Kanamori, H., J. Given, and T. Lay (1984), Analysis of seismic body waves excited by the Mount St. Helens eruption of May 18, 1980, *J. Geophys. Res.*, *89*(B3), 1856–1866.

Kanamori, H., J. Mori, E. Hauksson, T. Heaton, L. Hutton, and L. Jones (1993), Determination of earthquake energy release and ML using TERRAscope, *Bull. Seismol. Soc. Am.*, *83*(2), 330–346.

Koopmann, A. (2004), Magma mingling: The hydrodynamic genesis of magmatic dispersions, PhD Thesis, Inst. für Geol., Fac. für Geowissenschaften, Univ. Würzburg.

Kyle, P (1994), Preface, in *Volcanological and Environmental Studies of Mount Erebus, Antarctica, Antarct. Res. Ser.,* vol. 66, edited by P. Kyle, pp. xiii–xiv, AGU, Washington, D.C.

La Rocca, M., E. Del Pezzo, M. Simini, R. Scarpa, and G. De Luca (2001), Array analysis of seismograms from explosive sources: Evidence for surface waves scattered at the main topographical features, *Bull. Seismol. Soc. Am.*, *91*(2), 219–231, doi:10.1785/0120000028.

Lane, S. J., and J. S. Gilbert (eds.) (2008), *Fluid Motions in Volcanic Conduits: A Source of Seismic and Acoustic Signals,* Geological Society, London, Special Publications, 307, 147–167, doi:10.1144/SP307.90305-8719/08/$15.00.

Lighthill, J. (1978), *Waves in Fluids*, Cambridge Univ. Press, New York.

McGetchin, T., and B. Chouet (1979), Energy budget of the Volcano Stromboli, Italy, *Geophys. Res. Lett.*, *6*(4), 317–320.

Molina, I., A. Burgisser, and C. Oppenheimer (2012), Numerical simulations of convection in crystal-bearing magmas: A case study of the magmatic system at Erebus, Antarctica, *J. Geophys. Res.*, *117*, B07209, doi:10.1029/2011JB008760.

Neuberg, J., R. Luckett, M. Ripepe, and T. Braun (1994), Highlights from a seismic broadband array on Stromboli volcano, *Geophys. Res. Lett.*, *21*(9), 749–752.

Nishimura, T., and B. Chouet (2003), A numerical simulation of magma motion, crustal deformation, and seismic radiation associated with volcanic eruptions, *Geophys. J. Int.*, *153*(3), 699–718, doi:10.1046/j.1365-246X.2003.01936.x.

Oppenheimer, C., R. Moretti, P. Kyle, A. Escenbacher, J. Lowenstern, R. Hervig, and N. Dunbar (2011), Mantle to surface degassing of alkalic magmas at Erebus volcano, Antarctica, *Earth. Planet. Sci. Lett.*, *306*(3), 261–271, doi:10.1016/j.epsl.2011.04.005.

Oppenheimer, C., and P. Kyle (2008), Volcanology of Erebus volcano, Antarctica, *J. Volcanol. Geotherm. Res.*, *177*, v–vii, 3, doi:10.1016/j.jvolgeores.2008.10.006.

Parfitt, E. A. (2004), A discussion of the mechanisms of explosive basaltic eruptions, *J. Volcanol. Geotherm. Res.*, *134*, 77–107.

Pierce, A. (1981), *Acoustics: An Introduction to Its Physical Principles and Applications*, 678 pp., McGraw-Hill, New York.

Ripepe, M., and E. Marchetti (2002), Array tracking of infrasonic sources at Stromboli volcano, *Geophys. Res. Lett.*, *29*(22), 2076, doi:10.1029/2002GL015452.

Ripepe, M., M. Rossi, and G. Saccorotti (1993), Image processing of explosive activity at Stromboli, *J. Volcanol. Geotherm. Res.*, *54*, 335–351, doi:10.1016/0377-0273(93)90071-X.

Ripepe, M., E. Marchetti, P. Poggi, A. Harris, A. Fiaschi, and G. Ulivieri (2004), Seismic, acoustic, and thermal network monitors the 2003 eruption of Stromboli Volcano, *Eos Trans. AGU*, *85*(35), 329, doi:10.1029/2004EO350001.

Rowe, C., R. Aster, P. Kyle, J. Schlue, and R. Dibble (1998), Broadband recording of Strombolian explosions and associated very-long-period seismic signals on Mount Erebus Volcano, Ross Island, Antarctica, *Geophys. Res. Lett.*, *25*(13), 2297–2300.

Rowe, C., R. Aster, P. Kyle, R. Dibble, and J. Schlue (2000), Seismic and acoustic observations at Mt. Erebus Volcano, Ross Island, Antarctica, 1994–1998, *J. Volcanol. Geotherm. Res.*, *101*, 105–128.

Scharff, L., M. Hort, A. Harris, M. Ripepe, J. Lees, and R. Seyfried (2008), Eruption dynamics of the SW crater of Stromboli volcano, Italy—An interdisciplinary approach, *J. Volcanol. Geotherm. Res.*, *176*(4), 565–570, doi:10.1016/j.jvolgeores.2008.05.008.

Stepanishen, P. (1998), Transient radiation, in *Handbook of Acoustics*, edited by Crocker, M., pp. 119–126, Wiley-Interscience, New York.

Sweeney, D., P. R. Kyle, and C. Oppenheimer (2008), Sulfur dioxide emissions and degassing behavior of Erebus volcano, Antarctica, *J. Volcanol. Geotherm. Res.*, *177*(3), 725–733, doi:10.1016/j.jvolgeores.2008.01.024.

Taddeucci, J., P. Scarlato, A. Capponi, E. Del Bello, C. Cimarelli, D. Palladino, and U. Kueppers (2012), High-speed imaging of Strombolian explosions: The ejection velocity of pyroclasts, *Geophys. Res. Lett.*, *39*, L02301, doi:10.1029/2011GL050404.

Vergniolle, S. (1998), Modeling two-phase flow in a volcano, in *Proceedings of the Thirteenth Australasian Fluid Mechanics Conference*, edited by M. C. Thompson, and K. Hourigan, pp. 647–650, Monash University - Department of Mechanical Engineering, Victoria, 13–18 December.

Vergniolle, S., and G. Brandeis (1994), Origin of the sound generated by Strombolian explosions, *Geophys. Res. Lett.*, *21*(18), 1959–1962, doi:10.1029/94GL01286.

Vergniolle, S., and M. Mangan (2000), Hawaiian and Strombolian eruptions, in *Encyclopedia of Volcanoes*, edited by H. Sigurdsson et al., pp. 447–461, Academic Press, San Diego, Calif.

Vergniolle, S., G. Brandeis, and J.-C. Mareschal (1996), Strombolian explosions 2. Eruption dynamics determined from acoustic measurements, *J. Geophys. Res.*, *101*(B9), 20,449–20,466, doi:10.1029/96JB01925.

Vidal, V., J. Geminard, T. Divoux, and F. Melo (2006), Acoustic signal associated with the bursting of a soap film which initially closes an overpressurized cavity, *Eur. Phys. J. B.*, *54*(3), 321–339, doi:10.1140/epjb/e2006-00450-0.

Vidal, V., M. Ripepe, T. Divoux, D. Legrand, J. Géminard, and F. Melo (2010), Dynamics of soap bubble bursting and its implications to volcano acoustics, *Geophys. Res. Lett.*, *37*, L07302, doi:10.1029/2009GL042360.

Vöge, M., and M. Hort (2009), Installation of a Doppler radar monitoring system at Merapi volcano, Indonesia, *IEEE Trans. Geosci. Remote Sens.*, *47*(1), 251–271, doi:10.1109/TGRS.2008.2002693.

Walker, D., and O. Mullins Jr (1981), Surface tension of natural silicate melts from 1200°–1500°C and implications for melt structure, *Contrib. Mineral. Petrol.*, *76*, 455–462.

Webb, S., and D. Dingwell (1990), Non-Newtonian rheology of igneous melts at high stresses and strain rates: eExperimental results for rhyolite, andesite, basalt, and nephelinite, *J. Geophys. Res.*, *95*(B10), 15,695–15,701.

Zandomeneghi, D., R. Aster, P. Kyle, A. Barclay, J. Chaput, and H. Knox (2013), Internal structure of Erebus volcano, Antarctica imaged by high-resolution active-source seismic travel time and scattering tomography, *J. Geophys. Res. Solid Earth*, *118*, 1067–1078, doi:10.1002/jgrb.50073.